Mechanical Systems and Signal Processing 223 (2025) 111843

Contents lists available at ScienceDirect

Mechanical Systems and Signal Processing

journal homepage: www.elsevier.com/locate/ymssp

# Comprehensive analysis of a butterfly-shaped piezoelectric shunting vibration absorber for robust vibration reduction and isolation: Theoretical and experimental validation

Weiting Chen [a,b,d], Jiayu Lu [a,b], Xing Tan [a,b], Paolo Albertelli [d,e], Huan He [a,b,c,*]

[a] State Key Laboratory of Mechanics and Control of Mechanical Structures, Nanjing University of Aeronautics and Astronautics, Nanjing 210016, China
[b] Institute of Vibration Engineering Research, Nanjing University of Aeronautics and Astronautics, Nanjing 210016, China
[c] University of Chinese Academy of Sciences, Nanjing 211135, China
[d] Politecnico di Milano, Department of Mechanical Engineering, via La Masa, 1, Lombardy, Milan 20156, Italy
[e] MUSP Macchine Utensili Sistemi di Produzione, strada della Torre della Razza, Emilia-Romagna, Piacenza 29122, Italy

ARTICLE INFO

Communicated by Miguel Matos Neves

*Keywords:*
Piezoelectric shunting vibration absorber
Amplitude reduction
Vibration isolation
Various excitation conditions
Segmented inductance circuit

ABSTRACT

The Piezoelectric Shunting Vibration Absorber (PSVA) has garnered attention for its effectiveness in vibration control. This paper aims to propose a novel PSVA capable of simultaneously amplitude reduction and vibration isolation under various conditions. The PSVA consists of a butterfly-shaped link component and a piezoelectric stack, connected to the structure to be damped via bolts. Subsequently, an equivalent schematic diagram of the PSVA is established, and its equivalent stiffness is determined. Taking a single-degree-of-freedom structure as an example, considering the dynamic stiffness of the shunting circuit, a dynamic model of the electromechanical coupled system is developed, obtaining the system's acceleration response and force transmissibility frequency response functions. Following this, experimental equipment is designed and fabricated, and the performance of the PSVA is tested under various excitation conditions. Finally, inspired by the experimental results, a segmented inductance circuit is designed and tested for its capability to broaden the vibration control bandwidth.

## 1. Introduction

With the advancement of science and technology, the demands on the stability of engineering structures have become increasingly stringent. Unfortunately, inevitably strong vibrations often lead to structural damage, compromising the stability of the structure [1–3]. Traditional vibration control techniques, such as rubber dampers [4–6], while simple in construction and effective in energy absorption, suffer from limitations such as low stiffness, which can lead to frequency shifts in the main structure. Moreover, they are non-tunable and unsuitable for complex working environments, often prone to damage.

Subsequently, the concept of dynamic vibration absorbers, also known as tuned mass dampers (TMD), was proposed by Frahm [7], comprising mass-spring subsystems. The principle behind this approach is to tune the natural frequency of the subsystem to match that of the main structure, thereby utilizing the vibration of the subsystem to suppress vibrations in the main structure during resonance.

* Corresponding author at: State Key Laboratory of Mechanics and Control of Mechanical Structures, Nanjing University of Aeronautics and Astronautics, Nanjing 210016, China.
*E-mail address:* hehuan@nuaa.edu.cn (H. He).

https://doi.org/10.1016/j.ymssp.2024.111843
Received 29 May 2024; Received in revised form 13 August 2024; Accepted 14 August 2024
Available online 21 August 2024

Both Ikago et al. [8] and Garrido et al. [9] introduced a technique that integrates an inertial mass with a viscous mass damper, resulting in a tuned viscous mass damper (TVMD). The research of Hu [10,11] has demonstrated superior control effectiveness compared to conventional viscous dampers (VDs). They focus on optimizing the $H_2$ and $H_\infty$ performance for inerter-based dynamic vibration absorbers (IDVAs). The IDVAs proposed herein replace the damper in traditional dynamic vibration absorbers (TDVAs) with inerter-based mechanical networks. However, traditional TMDs also have drawbacks. For instance, they involve significant additional mass, which can cause frequency shifts in the main structure. While they offer tunability, practical implementation is complex, requiring adjustments to the mass of the subsystem. Furthermore, they impose high demands on installation environments. Some researchers have also made improvements on the TMDs. Manzoni et al [12] introduces the Shape Memory Alloy Tuned Mass Damper (SMA-TMD). The SMA-TMD system performs better in comparison to the TMD system. They developed the models of the two layouts (wire-based and beam-based) to compare these two main layouts in terms of adaptation capability, exerted force and electrical power consumption.

Later, it was discovered that smart materials could effectively address these issues. Wherein, the piezoelectric materials [13–15] is one of the most widely used devices for the passive vibration control of structures. Passive piezoelectric vibration control is also known as the technique of piezoelectric shunt damping. When incorporating piezoelectric materials into traditional TMDs, the electromechanical coupling characteristics of piezoelectric materials, along with the inertia, stiffness, and damping properties of the shunt circuit, can replace the mass, spring, and damping components of traditional TMDs. The small added mass minimizes their impact on the system, while their fast dynamic response high specific force, and wide broadband enable these actuators to perform low and high-frequency vibration suppression [16–18]. The development of piezoelectric shunting vibration absorber (PSVA) can generally be divided into three parts: new structures [19–23], novel circuits [24–27], and designs integrating with other concepts [28–30]. Currently, in order to achieve effective application of PSVA in practical engineering, the following challenges still need to be overcome.

- The characteristic of piezoelectric stacking being unable to withstand shear forces necessitates an external protective frame to shield it from such forces, while also allowing the piezoelectric power shunt absorber to interface with the damped object and function seamlessly in various installation environments.
- Additionally, many studies on PSVAs only test the vibration suppression effects under specific excitation conditions, such as random excitation [31], sine excitation [32], with limited comprehensive testing of the proposed PSVA under various excitations. Hence, it is essential to develop a PSVA that can effectively control vibrations under various excitation conditions containing random, sine and impact ones.
- Moreover, vibration control effects can be categorized into vibration isolation and amplitude attenuation aspects. For instance, the research of Lin et al. [33] only focuses on isolation. It is urgently needed to propose a PSVA that simultaneously achieves both objectives.
- At last, broadening the vibration control bandwidth is also a crucial technological point for PSVA. According to the principle of PSVA, vibration at resonance frequencies is effectively suppressed, but the phenomenon of increased vibration in non-resonant regions is often overlooked. Some researchers have attempted to improve this deficiency, with who introducing a semi-active control method – adaptive circuit, and simulation results and simple experiment verifying the broadband vibration reduction effect of this circuit [34]. However, the time delay issue introduced by the adaptive circuit may lead to poor effectiveness in practical applications. Furthermore, complex circuit control systems also introduce extra weight and demand more installation space, which is undesirable. Therefore, this study will struggle to address the aforementioned challenges and issues by conducting the following research.

This research aims at developing a novel butterfly-shaped vibration control device with piezoelectric materials to address the above-mentioned issues. In this study, the static and dynamic models of the electromechanical coupling system are presented. A comprehensive testing system was developed, incorporating Single-degree-of-freedom spring-mass system alongside the designed PSVA. The efficacy of the PSVA was evaluated through sweep sine testing both numerically and experimentally when comparing the PSVA's performance in open-circuit versus connected-circuit states, demonstrating remarkable amplitude reduction and vibration isolation capabilities. Furthermore, a series of diverse excitation conditions, including random excitation, impact excitation, and single-frequency excitation, were applied during testing to showcase the versatility of the PSVA. Through a thorough parameter analysis, the impact of inductance values on vibration control effectiveness was examined, offering invaluable insights for PSVA applications. Building upon insights gained from single-frequency tests, a novel segmented inductance circuit was introduced to enhance the effective vibration control bandwidth of the PSVA.

## 2. Modelling

This section mainly introduces the configuration of the proposed novel piezoelectric shunt vibration absorber (PSVA). The static stiffness of this configuration is obtained through the application of the Castigliano's 2nd theorem. Subsequently, the Laplace transform is introduced to discuss the equivalent dynamic stiffness of the piezoelectric stack who is connected to the shunt circuit. Then, combined with static analysis, the overall dynamic stiffness of the proposed PSVA can be determined. Using a single-degree-of-freedom system as an example, the force transmissibility and amplitude frequency response of the entire system can be obtained, facilitating a simulation-based discussion on the performance of this PSVA.

### 2.1. Description of the designed PSVA

This paper aims to propose a novel piezoelectric shunt dynamic vibration absorber, consisting of a butterfly-shaped steel frame and a stack of piezoelectric elements as Fig. 1 (a) shows. Compared to traditional piezoelectric plates or fibers, piezoelectric stacks offer higher energy density and a broader frequency response range, making them more efficient in vibration control. Additionally, piezoelectric stacks have a longer lifespan and greater reliability, reducing maintenance needs and costs compared to piezoelectric plates. However, due to its layered structure, piezoelectric stacks cannot withstand shear forces. Therefore, in practical applications, a protective outer frame is required to shield them from shear forces. Hence, inspired by the rhombic frame structure in Ref. [35], the butterfly-shaped structure is designed to protect the piezoelectric stack during the vibration reduction process. The assembly containing the butterfly-shaped frame and piezoelectric stack can serve as a vibration control unit and can be attached to the vibrating object, such as bending beams via bolts. Due to its compact structure and easy installation, it can be flexibly positioned and scaled according to specific requirements, making it suitable for various working conditions. Using a single-degree-of-freedom system as an example, this paper validates the performance of the designed dynamic vibration absorber.

### 2.2. Static analysis

The bending and axial stress in the diagonal bar can be separately written as:

$$\sigma_{m-yy} = \frac{(F_N\cos\beta - F\sin\beta)(l_1 - x) + M}{I_1} y$$
$$\sigma_{m-xx} = \frac{(F_N\sin\beta + F\cos\beta)}{A_1} \tag{1}$$

The axial stress of the piezoelectric stack is defined as:

$$\sigma_{p-xx} = \frac{F_N}{A_2} \tag{2}$$

The total strain energy of this piezoelectric butterfly-shaped structure has the following form:

$$U = U_{bending} + U_{axial} = \int_V \frac{1}{2}\left(\sigma_{xx}^2 + \sigma_{yy}^2\right) \mathrm{d}V \tag{3}$$

$$U = \frac{2l_1^3}{3E_1I_1}(F_N\cos\beta - F\sin\beta)^2 + \frac{2M^2 l_1}{E_1I_1} + \frac{2M(F_N\cos\beta - F\sin\beta)l_1^2}{E_1I_1} + \frac{2(\sin\beta + F\sin\beta)^2 l_1}{E_1A_1} + \frac{2F_N^2 l_2}{E_2A_2} \tag{4}$$

According to Castigliano's 2nd theorem, for this linear conservative system, the generalized displacement, which is defined as the first partial derivative of the strain energy concerning generalized force, is set to 0. Hence, Castigliano's 2nd theorem is presented as follows:

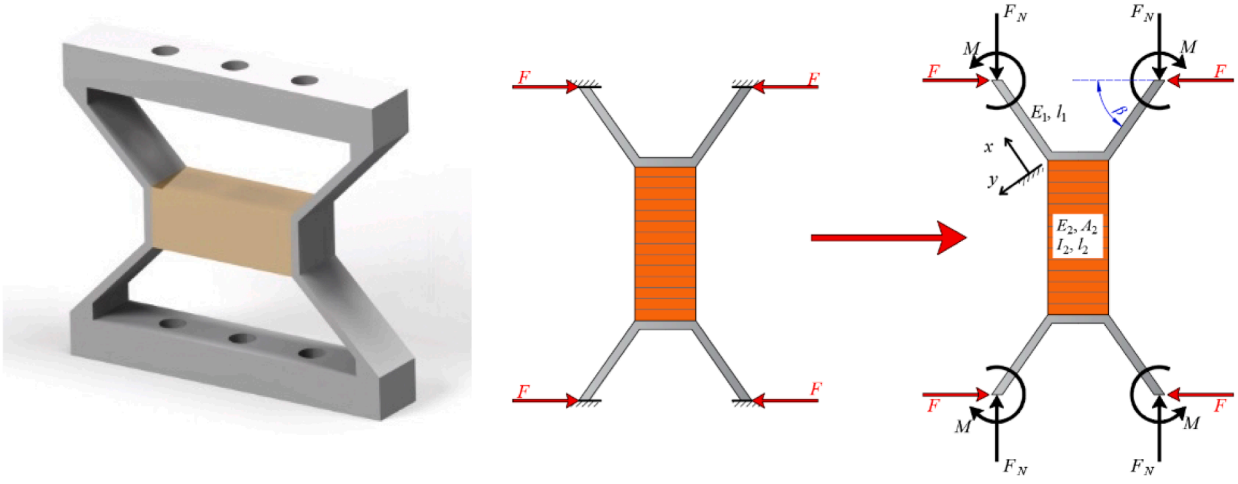


(a) Diagram of the designed PSVA (b) Force analysis diagram

**Fig. 1.** Schematic diagram of the designed PSVA.

$$\begin{cases} \dfrac{\partial U}{\partial F_N} = 0 \\ \dfrac{\partial U}{\partial M} = 0 \end{cases} \tag{5}$$

The solutions of Eq. (5) are given as:

$$\begin{cases} F_N = \dfrac{l_1^3 \sin\beta\cos\beta/3E_1I_1 - 4l_1\sin\beta\cos\beta/E_1A_1}{4l_2/E_2A_2 + l_1^3\cos^2\beta/3E_1I_1 + 4l_1\sin^2\beta/E_1A_1} F = XF \\ M = \dfrac{2l_1\sin\beta/E_1A_1 + 2l_2\sin\beta/E_2A_2}{4l_2/E_2A_2 + l_1^3\cos^2\beta/3E_1I_1 + 4l_1\sin^2\beta/E_1A_1} Fl_1 = YFl_1 \end{cases} \tag{6}$$

Substituting Eq. (6) into Eq. (4), the expression of the total strain energy is obtained as:

$$U = \frac{2}{3}F^2\left[\frac{3l_2X^2}{E_2A_2} + \frac{3l_1^3Y^2}{E_1I_1} + \frac{3l_1^3Y(X\cos\beta - \sin\beta)}{E_1I_1} + \frac{l_1^3Y(-X\cos\beta + \sin\beta)^2}{E_1I_1} + \frac{3l_1(X\sin\beta + \cos\beta)^2}{E_1A_1}\right] \tag{7}$$

According to the classical theory of mechanics, the following definitions are given:

$$k_{mc} = E_1A_1/l_1, k_{mb} = E_1I_1/l_1^3, k_2 = E_2A_2/l_2 \tag{8}$$

where $k_{mc}$ and $k_{mb}$ are the compressing and bending stiffness respectively. $k_2$ is the static compressing stiffness of the piezoelectric stack.

$$U = 2F^2\left\{\frac{2k_2 + [12k_{mb}(-1 + \cos2\beta) + k_{mc}(1 - \cos2\beta)]}{24k_{mb}k_{mc} + k_2[12k_{mb}(1 - \cos2\beta) + k_{mc}(1 + \cos2\beta)]}\right\} \tag{9}$$

The following expression can be derived according to Castigliano's 2nd theorem:

$$\Delta_F = \frac{\partial U}{\partial F} = 4F\left\{\frac{2k_2 + [12k_{mb}(-1 + \cos2\beta) + k_{mc}(1 - \cos2\beta)]}{24k_{mb}k_{mc} + k_2[12k_{mb}(1 - \cos2\beta) + k_{mc}(1 + \cos2\beta)]}\right\} \tag{10}$$

The stiffness of this butterfly-shaped structure is written as:

$$k_a = \frac{2F}{2\Delta_F} = \frac{24k_{mb}k_{mc} + k_2[12k_{mb}(1 - \cos2\beta) + k_{mc}(1 + \cos2\beta)]}{2k_2 + 12k_{mb}(-1 + \cos2\beta) + k_{mc}(1 - \cos2\beta)} \tag{11}$$

### 2.3. Dynamic analysis

To illustrate the effect of this butterfly-shaped structure with a piezoelectric stack, we consider a single-degree-of-freedom host system containing an equivalent mass $m$ here as Fig. 2 shows. The piezoelectric structure is equivalent to a spring $k_a$ and damping $c_a$ under the one degree of freedom system hypothesis. When dynamic force is applied to this structure, simply considering the static stiffness of piezoelectric components is not enough. When the piezoelectric stack is connected to a shunt circuit, the impedance of the circuit should also be considered. The constitutive equation of the piezoelectric stack is given as:

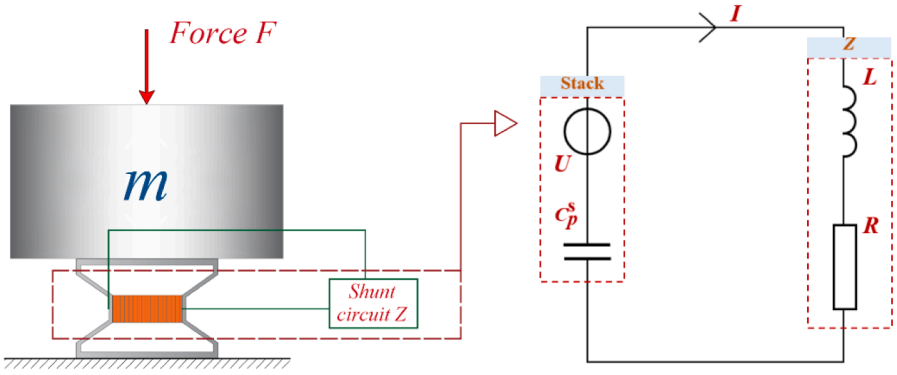


**Fig. 2.** Schematic diagram of the electromechanical coupling system.

$$\begin{bmatrix} q \\ f \end{bmatrix} = \begin{bmatrix} C_p^S & \theta_p \\ \theta_p & k_2 \end{bmatrix} \begin{bmatrix} v \\ x \end{bmatrix} \tag{12}$$

where $q$, $v$ represents the generated charge and voltage of the piezoelectric stack respectively, while $f$, $x$ represents the applied force and the contraction of the stack. $C_p^S$ is the capacitance of the piezoelectric stack without deformation and $\theta_p$ is the generalized electromechanical coupling coefficient of the piezoelectric stack. Transforming Eq. (12) into the Laplace domain and integrating it yields the following expression:

$$\begin{cases} I(s) = sQ(s) = sC_p^S V(s) + s\theta_p X(s) \\ F(s) = -\theta_p V(s) + k_2 X(s) \end{cases} \tag{13}$$

In which $s$ represents the Laplace variable, and $I(s)$ denotes the current through the piezoelectric stack and $V(s)$ is the voltage of the stack. According to Kirchhoff's law, the following equation can be obtained:

$$V + I \cdot Z = 0 \tag{14}$$

where $Z$ is the impedance of the shunting circuit. Combining Eq. (14) and Eq. (13), the equivalent dynamic stiffness can be derived as shown in Eq. (15).

$$k_{2d}(s) = \frac{F(s)}{X(s)} = k_2 + \frac{s\theta_p^2 Z}{sC_p^S Z + 1} \tag{15}$$

Substituting Eq. (15) into Eq. (11), the dynamic stiffness of this vibration control device can be obtained as

$$k_a(s) = \frac{24k_{mb}k_{mc} + Pk_2 + sZ\left[24k_{mb}k_{mc}C_p^S + P\left(k_2 C_p^S + \theta_p^2\right)\right]}{2k_2 + Q + sZ\left(2k_2 C_p^S + 2\theta_p^2 + QC_p^S\right)} \tag{16}$$

where

$$\begin{aligned} P &= 12k_{mb}(1 - \cos 2\beta) + k_{mc}(1 + \cos 2\beta) \\ Q &= 12k_{mb}(-1 + \cos 2\beta) + k_{mc}(1 - \cos 2\beta) \end{aligned} \tag{17}$$

Then the acceleration response of the host system can be gained as

$$A(s) = \frac{s^2 F(s)}{ms^2 + cs + k_a(s)} \tag{18}$$

And the force transmissibility can also be derived as

$$F_T(s) = \frac{F_{out}}{F_{in}} = \frac{k_a(s)}{ms^2 + cs + k_a(s)} \tag{19}$$

where $m$, $c$ is the mass and the damping coefficient of host system respectively. Here, the expressions for the system's force transmissibility and amplitude frequency response have been obtained. The optimal shunt circuit parameters will be derived in the following parts.

### 2.4. Derivation of the optimal parameters of the shunt circuit

In this paper, we focus on the vibration control performance of the proposed absorber when it is shunted with a series $RL$ circuit. The impedance $Z(s)$ has the form $sL+R$, where $L$ and $R$ denote the inductance and resistance values, respectively. Substituting $Z(s)$ into Eq. (16), and note that $s = \mathrm{j}\omega$ (j is the imaginary unit, and $\omega$ is the excitation frequency), the expression of the dynamic stiffness can be rewritten as

$$k_a(\omega) = \frac{24k_{mb}k_{mc} + Pk_2 + \mathrm{j}\omega(\mathrm{j}\omega L + R)\left[24k_{mb}k_{mc}C_p^S + P\left(k_2 C_p^S + \theta_p^2\right)\right]}{2k_2 + Q + \mathrm{j}\omega(\mathrm{j}\omega L + R)\left(2k_2 C_p^S + 2\theta_p^2 + QC_p^S\right)} \tag{20}$$

According to Hagood and Flotow's work [36], a piezoelectric absorber shunted with a series $RL$ circuit can be regarded as a dynamic vibration absorber. The fixed-points method can then be used to derive the exact solutions for the optimal circuit parameters. Yamada et al. [37] also employed this method to derive the optimal parameters for the shunt circuit. Through simulation and experimentation, they validated the effectiveness of this method. It is important to note that this method is only suitable for analyzing the undamped or slightly damped host systems. Given that the proposed electromechanical coupling system meets the slightly damped condition, mechanical damping is neglected (i.e., $c = 0$) in the following theoretical derivation, and the fixed-points method is applied.

Combining Eqs. (20) and (19), the detailed expression of the force transmissibility can be represented as

$$F_T(\omega) = \frac{M_1 + \mathrm{j}N_1}{M_2 + \mathrm{j}N_2} \tag{21}$$

where

$$\begin{aligned} M_1 &= 24k_{mb}k_{mc} + k_2P - 24C_p^S k_{mb}k_{mc}L\omega^2 - C_p^S k_2 LP\omega^2 - LP\theta_p^2\omega^2, \\ N_1 &= 24C_p^S k_{mb}k_{mc}R\omega + C_p^S k_2 PR\omega + PR\theta_p^2\omega, \\ M_2 &= 24k_{mb}k_{mc} + k_2P - 24C_p^S k_{mb}k_{mc}L\omega^2 - 2k_2m\omega^2 - C_p^S k_2 LP\omega^2 \\ &\quad -mQ\omega^2 - LP\theta_p^2\omega^2 + 2C_p^S k_2 Lm\omega^4 + C_p^S LmQ\omega^4 + 2Lm\theta_p^2\omega^4, \\ N_2 &= 24C_p^S k_{mb}k_{mc}R\omega + C_p^S k_2 PR\omega + PR\theta_p^2\omega - 2C_p^S k_2 mR\omega^3 - C_p^S mQR\omega^3 - 2mR\theta_p^2\omega^3. \end{aligned}$$

The square of the absolute value of the force transmissibility can be written in the form of

$$|F_T(\omega)|^2 = \frac{a_1^2\omega^2 \cdot R^2 + (a_2 - La_1\omega^2)^2}{\omega^2(a_1 - a_3\omega^2)^2 \cdot R^2 + (a_2 - La_1\omega^2 - a_4\omega^2 + La_3\omega^4)^2} \tag{22}$$

where

$$\begin{aligned} a_1 &= 24C_p^S k_{mb}k_{mc} + P\left(k_2C_p^S + \theta_p^2\right), \\ a_2 &= 24k_{mb}k_{mc} + k_2P, \\ a_3 &= 2m\left(k_2C_p^S + \theta_p^2\right) + mC_p^S Q, \\ a_4 &= 2mk_2 + mQ. \end{aligned}$$

According to the fixed-point method, once the inductance $L$ is given, the response curves for different resistance $R$ all pass through two fixed points, $\Lambda_1$ and $\Lambda_2$. When the response values at these two fixed points are equal and reach their maximum, the system response is minimized. The corresponding inductance $L$ and resistance $R$ is thus optimal. First, let's derive the optimal inductance $L$. Since the locations of fixed points on the horizontal axis are independent of the resistance $R$, the following expression can be obtained from Eq. (22):

$$\frac{a_1^2\omega^2}{\omega^2(a_1 - a_3\omega^2)^2} = \frac{(a_2 - La_1\omega^2)^2}{(a_2 - La_1\omega^2 - a_4\omega^2 + La_3\omega^4)^2} \tag{23}$$

Then an equation related to $\omega$ can be derived as follows:

$$2a_1a_3\omega^4L - (a_2a_3 + a_1a_4 + 2a_1^2L)\omega^2 + 2a_1a_2 = 0 \tag{24}$$

Its solutions are given as:

$$\omega_{\Lambda_1,\Lambda_2} = \sqrt{\frac{a_2a_3 + a_1a_4 + 2a_1^2L \pm \sqrt{-16a_1^2a_2a_3L + (a_2a_3 + a_1a_4 + 2a_1^2L)^2}}{4a_1a_4L}} \tag{25}$$

Substituting Eq. (25) into Eq. (22), the response values at these two fixed points are given by:

$$\begin{cases} |F_T(\omega_{\Lambda_1})|^2 = \dfrac{a_1^2R^2\omega_{\Lambda_1}^2 + \left(a_2 - La_1\omega_{\Lambda_1}^2\right)^2}{R^2\omega_{\Lambda_1}^2\left(a_1 - a_3\omega_{\Lambda_1}^2\right)^2 + \left(a_2 - La_1\omega_{\Lambda_1}^2 - a_4\omega_{\Lambda_1}^2 + La_3\omega_{\Lambda_1}^4\right)^2}, \\ |F_T(\omega_{\Lambda_2})|^2 = \dfrac{a_1^2R^2\omega_{\Lambda_2}^2 + \left(a_2 - La_1\omega_{\Lambda_2}^2\right)^2}{R^2\omega_{\Lambda_2}^2\left(a_1 - a_3\omega_{\Lambda_2}^2\right)^2 + \left(a_2 - La_1\omega_{\Lambda_2}^2 - a_4\omega_{\Lambda_2}^2 + La_3\omega_{\Lambda_2}^4\right)^2} \end{cases} \tag{26}$$

They must be equal, leading to the following expression:

$$|F_T(\omega_{\Lambda_1})|^2 = |F_T(\omega_{\Lambda_2})|^2 \tag{27}$$

Then the equation associated with inductance $L$ yields

$$(a_2a_3 + a_1(a_4 - 2a_1L))\sqrt{-16a_1^2a_2a_3L + (a_2a_3 + a_1(a_4 + 2a_1L))^2} = 0 \tag{28}$$

By solving it and discarding the negative solutions, the optimal inductance $L$ can be expressed analytically as:

$$L_{\text{opt}} = \frac{a_2 a_3 + a_1 a_4}{2a_1^2} \tag{29}$$

Subsequently, by adjusting the resistance $R$ to make $|F_T(\omega)|^2$ reach its maximum at the first fixed point (or the second one), the optimal resistance $R$ can be determined. Defining that

$$|F_T(\omega)|^2 = \frac{F_{\text{num}}}{F_{\text{den}}}, \tag{30}$$

where

$$F_{\text{num}} = a_1^2 R^2 \omega^2 + \left(a_2 - L a_1 \omega^2\right)^2, F_{\text{den}} = R^2\omega^2\left(a_1 - a_3\omega^2\right)^2 + \left(a_2 - L a_1\omega^2 - a_4\omega^2 + L a_3 \omega^4\right)^2 \tag{31}$$

The derivative of $|F_T(\omega)|^2$ with respect to $\omega$ is given as

$$\frac{\partial |F_T(\omega)|^2}{\partial \omega} = \frac{\frac{\partial F_{\text{num}}}{\partial \omega} F_{\text{den}} - F_{\text{num}} \frac{\partial F_{\text{den}}}{\partial \omega}}{F_{\text{den}}^2} \tag{32}$$

Obviously, $F_{\text{den}} \neq 0$. By setting the numerator of Eq. (32) to zero, and substituting the locations of the two fixed points $\omega_{\Lambda_1}, \omega_{\Lambda_2}$ along with the optimal inductance $L_{\text{opt}}$ into Eq. (32), the optimal resistance $R$ can be obtained as

$$R = \frac{1}{2}\sqrt{r_1\left(r_2 + \sqrt{r_3(r_4 + r_5 + r_6 + r_7)}\right)} \tag{33}$$

where

$$r_1 = \frac{1}{a_1^2 a_3 \omega_{\Lambda_1}^4\left(a_1 - a_3\omega_{\Lambda_1}^2\right)},$$

$$r_2 = 3a_2^2 a_3^2 \omega_{\Lambda_1}^4 + 2a_1^3 L_{\text{opt}} \omega_{\Lambda_1}^4\left(a_4 - 2a_3 L_{\text{opt}}\omega_{\Lambda_1}^2\right) - 4a_1 a_2 \omega_{\Lambda_1}^2\left(a_2 + a_3 L_{\text{opt}}\omega_1^4\right) + a_1^2\omega_{\Lambda_1}^4\left(a_4^2 - 4a_3 a_4 L_{\text{opt}}\omega_{\Lambda_1}^2 + 2a_3 L_{\text{opt}}\left(3a_2 + 2a_3 L_{\text{opt}}\omega_{\Lambda_1}^4\right)\right),$$

$$r_3 = (a_2 a_3 - a_1 a_4)\omega_{\Lambda_1}^4,$$

$$r_4 = 9a_2^3 a_3^3 \omega_{\Lambda_1}^4 - 4a_1^5 L_{\text{opt}}^2 \omega_{\Lambda_1}^4\left(a_4 - 4a_3 L_{\text{opt}}\omega_{\Lambda_1}^2\right) - 3a_1 a_2^2 a_3^2 \omega_{\Lambda_1}^2\left(8a_2 - 3a_4\omega_{\Lambda_1}^2 + 8_{a3} L_{\text{opt}}\omega_{\Lambda_1}^4\right),$$

$$r_5 = a_1^2 a_2 a_3\left(16a_2^2 - 8a_2 a_4\omega_{\Lambda_1}^2 - a_4^2\omega_{\Lambda_1}^4 + 36a_2 a_3 L_{\text{opt}}\omega_{\Lambda_1}^4 + 8a_3^2 L_{\text{opt}}^2\omega_{\Lambda_1}^8\right),$$

$$r_6 = a_1^3\left(-16a_2^2 a_3 L_{\text{opt}}\omega_{\Lambda_1}^2 - a_4^3\omega_{\Lambda_1}^4 + 8a_3 a_4^2 L_{\text{opt}}\omega_{\Lambda_1}^6 + 8a_2 a_3^2 L_{\text{opt}}^2\omega_{\Lambda_1}^6 - 24a_3^2 a_4 L_{\text{opt}}^2\omega_{\Lambda_1}^8 + 16a_3^3 L_{\text{opt}}^3\omega_{\Lambda_1}^{10}\right),$$

$$r_7 = -4a_1^4 L_{\text{opt}}\omega_{\Lambda_1}^4\left(a_4^2 - 6a_3 a_4 L_{\text{opt}}\omega_{\Lambda_1}^2 + a_3 L_{\text{opt}}\left(3a_2 + 8a_3 L_{\text{opt}}\omega_{\Lambda_1}^4\right)\right).$$

Up to this point, the analytical expressions of the optimal circuit parameters for force transmissibility have been derived. Through simulation, it is found that the acceleration response also demonstrates the optimal state under this optimal solution, so no additional deduction is required. The following simulation and experiment will use this optimal solutions. Subsequently, the experiments will be designed to acquire experimental results and validate the effectiveness of the proposed PSVA alongside simulation results.

## 3. Description of experimental setup

The diagram in Fig. 3 illustrates the conceptual overview of the experimental set up, comprising the host structure, a physical

**Table 1**
Parameters of the electromechanical coupling system.

| Property | Symbol | Value | Unit |
|---|---|---|---|
| Mass of host system | $m$ | 16 | kg |
| Compressing stiffness | $k_{\text{mc}}$ | $8.75 \times 10^3$ | N/m |
| Bending stiffness | $k_{\text{mb}}$ | $1.05 \times 10^8$ | N/m |
| Static compressing stiffness of the piezoelectric stack | $k_2$ | $1.197 \times 10^8$ | N/m |
| Electromechanical coupling factor | $\theta_P$ | 0.33 | C/m (N/V) |
| The capacitance of the piezoelectric stack | $C_P^S$ | 0.375 | μF |
| The angle of link part | $\beta$ | 45 | ° |

representation of the designed PSVA, a shunting circuit diagram, and data acquisition equipment. The host structure is composed of mass blocks, connected to the foundation through a straight guide rod. The straight guide rod primarily serves the purpose of stabilizing the structure. The designed PSVA is connected to the mass block and foundation through bolts. The relevant parameters involved in the experiment are listed in Table 1. Electrical wires are soldered to both ends of the piezoelectric stack electrodes, and they are connected to the shunting circuit. The measurement device primarily consists of an accelerometer on the mass block, force sensors 1 and 2. Two force sensors are used to obtain the force transmissibility of the system. Sensor 1 is connected to the exciter to measure the input force, while sensor 2 is positioned between the foundation and the mass block to measure the output force. A M+p system is used to manage the excitation and the acquisition of the temporal signals.

During the experiment, a common circuit configuration of a series circuit with resistance and inductance is employed, achieved through the use of an inductor box and a resistor box. Wherein, substituting the exact value of the relevant parameters into Eq. (29) & Eq. (33), the optimal condition of the shunt circuit is calculated as:

$$L_{\text{opt}} = 0.47\text{H}, R_{\text{opt}} = 51\Omega \tag{34}$$

## 4. Frequency domain performance of PSVA

### 4.1. Optimal performance of the designed PSVA

Primarily, we delved into the behavior of the vibration absorber under swept frequency excitation, which is a prevalent condition across diverse research studies. By scrutinizing the frequency response curves pre and post connection to the optimal shunt circuit, the performance of the vibration absorber can be distinctly validated. Taking into account the natural frequency of the single degree of freedom main system, which stands at 123 Hz, we designate the sweep range as [80, 180 Hz]. In order to fully showcase the effectiveness of the designed PSVA, the following discussion will unfold from two perspectives: acceleration and force transmissibility. The numerical simulation and experimental results are outlined as Figs. 4-7 show.

Figs. 4-5 present the amplitude frequency response of acceleration and transmissibility separately and Figs. 6 and 7 present the phase frequency response of acceleration and transmissibility respectively under open-circuit condition and optimal-circuit condition. As illustrated in Figs. 4-7, there was good agreement between the numerical and the experimental results both of the amplitude responses of acceleration and force transmissibility. They exhibit congruence in both peak magnitudes and overall curve trends. So do the phase responses of simulation and experiment. The subtle discrepancies between the simulation and experiment are that the frequency value corresponding to the double peaks of the amplitude curve and the frequency value corresponding to the inflection point of the phase curve have errors under the with-control condition. The experimental values of these two frequencies are slightly larger than the simulated ones. The excellent agreement between simulation and experiment validates the reliability of our simplified model.

Moreover, Figs. 4-5 exhibit the excellent vibration reduction effect of the designed PSVA. Compared with the open-circuit situation, when the system is assembled with PSVA connected to the optimal circuit, the simulated acceleration amplitude is reduced from 2.3 g to 0.38 g, the acceleration vibration reduction effect reaches 83.4 %, and the simulated force transmissibility amplitude is reduced

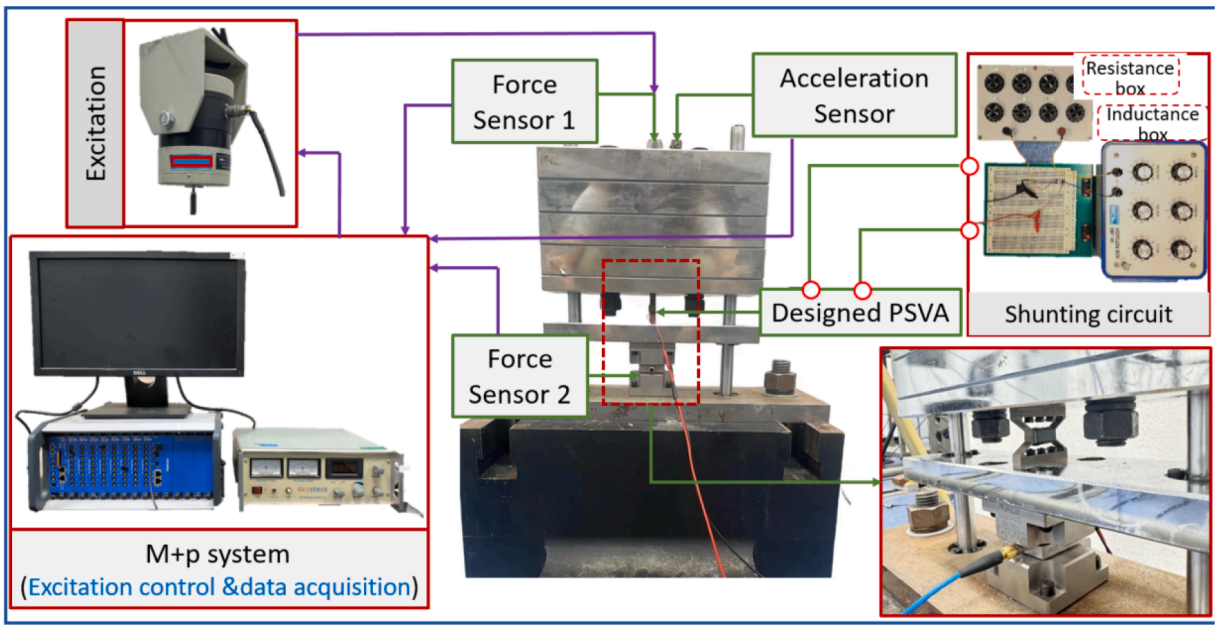


**Fig. 3.** Diagram of experimental setup.

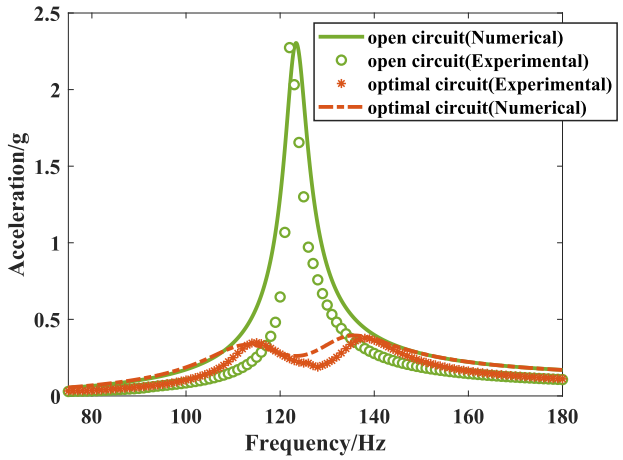


**Fig. 4.** Acceleration amplitude response of the host system under blue line: open circuit; orange line: $L$=0.47H, $R$=100 Ω. (For interpretation of the references to color in this figure legend, the reader is referred to the web version of this article.)

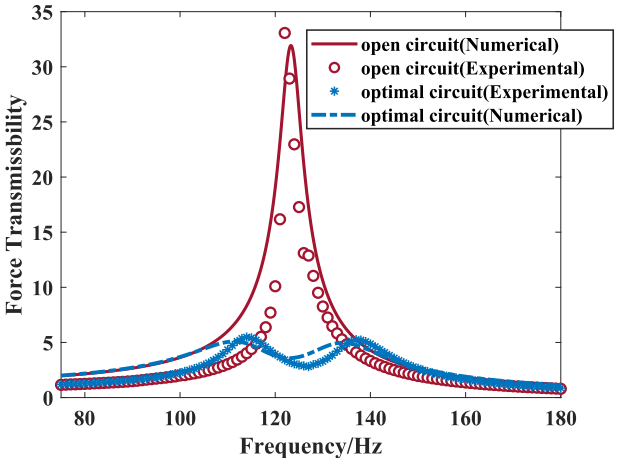


**Fig. 5.** Force transmissibility amplitude of the host system under blue line: open circuit; orange line: $L$=0.47H, $R$=100 Ω. (For interpretation of the references to color in this figure legend, the reader is referred to the web version of this article.)

from 31.8 to 5. The vibration reduction effect reaches 84.2 %. The experimental acceleration amplitude was reduced from 2.27 g to 0.38 g, and the acceleration vibration reduction effect reached 83.3 %. The force transmissibility amplitude in the experiment was reduced from 33.07 to 5.08, and the vibration reduction effect reached 84.6 %. These performances are excellent. It can be seen that the PSVA proposed here can well suppress the surface vibration of the system and reduce the force transmitted to the foundation at the same time.

### *4.2. Parametric analysis*

Then we discussed the performance of PSVA under different inductance conditions. Figs. 8 and 9 show the amplitude-frequency and phase-frequency response curves of acceleration and force transmissibility under different inductance values. Comparing Figs. 8 and 9, it can be seen that the acceleration and force transmissibility response curves change with inductance in a similar trend. Taking the acceleration response as an example, Fig. 8(a) and 8(c) are the simulated amplitude-frequency and phase-frequency response diagrams, and Fig. 8(b) and 8(d) are the experimental ones.

In comparison with Fig. 8(a) and 8(b), we can see that the curve trends of the experiment and simulation are consistent. As the inductance value increases, the first peak of the response curve (the one with the smaller resonance frequency) decreases. The second peak (the one with the larger resonant frequency) increases. This means that when the inductance value is small, the acceleration response is larger in low the frequency band and smaller in the high frequency band. When the inductance value is larger, the conclusion is opposite. It can be known from this that when the inductance value in the shunt circuit is small, the designed PSVA has a

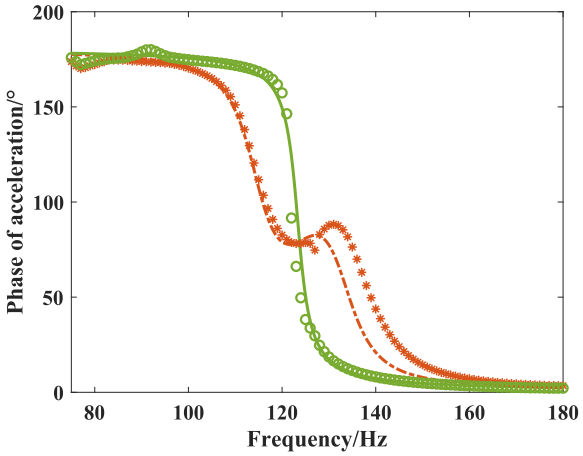


**Fig. 6.** Acceleration phase response of the host system under the blue line: open circuit; orange line: $L$=0.47H, $R$=100 Ω. (For interpretation of the references to color in this figure legend, the reader is referred to the web version of this article.)

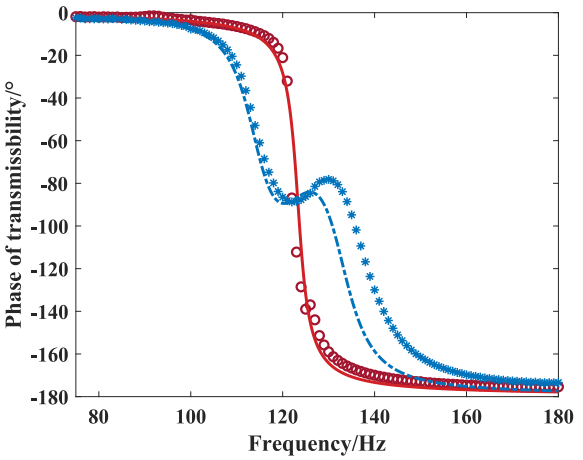


**Fig. 7.** Force transmissibility phase of the host system under the blue line: open circuit; orange line: $L$=0.47H, $R$=100 Ω. (For interpretation of the references to color in this figure legend, the reader is referred to the web version of this article.)

better effect on reducing the amplitude response in the high frequency band and a poor effect in the low frequency band. On the contrary, when the inductance value in the shunt circuit is large, the designed PSVA has a better effect on reducing the amplitude response in the low frequency band and a poor effect in the high frequency band. To clearly illustrate this point, a 2D plot of the inductance response graph is provided, as shown in Fig. 10. The darker the curve, the larger the inductance value. From the figure, it can be observed that on the left side of the center line, which corresponds to lower excitation frequencies, the system response decreases as the inductance value increases. Conversely, on the right side of the center line, which corresponds to higher excitation frequencies, the system response decreases as the inductance value decreases. This also supports the aforementioned argument: in the low-frequency band, higher inductance values provide a better overall amplitude attenuation effect, while in the high-frequency band, lower inductance values offer a better overall amplitude attenuation effect. A similar conclusion about the effect of the designed PSVA on isolating the force transmissibility can be obtained.

Hence, the conclusion can be gained that, both for isolating the force transmissibility and attenuating amplitude, the designed PSVA behaves better in the higher frequency band when the value inductance is smaller and has a better effect in the lower frequency band when the value inductance is larger. These conclusions can be a guide in the engineering application of PSVA.

Meanwhile, it can be observed that the two bone lines (the lines connecting the resonance peaks at different inductance values) are not perpendicular to the frequency coordinate axis, which indicates that as the inductance value changes, the time for resonance to occur will also change. For example, it can be seen from Fig. 8(b) and 8(d) that the first inflection point of the phase is similar in size, and the peak value of the second inflection point increases as the inductance increases. In order to more clearly demonstrate the performance changes of PSVA under different inductance values, we extracted the peak data of the above three-dimensional graph and

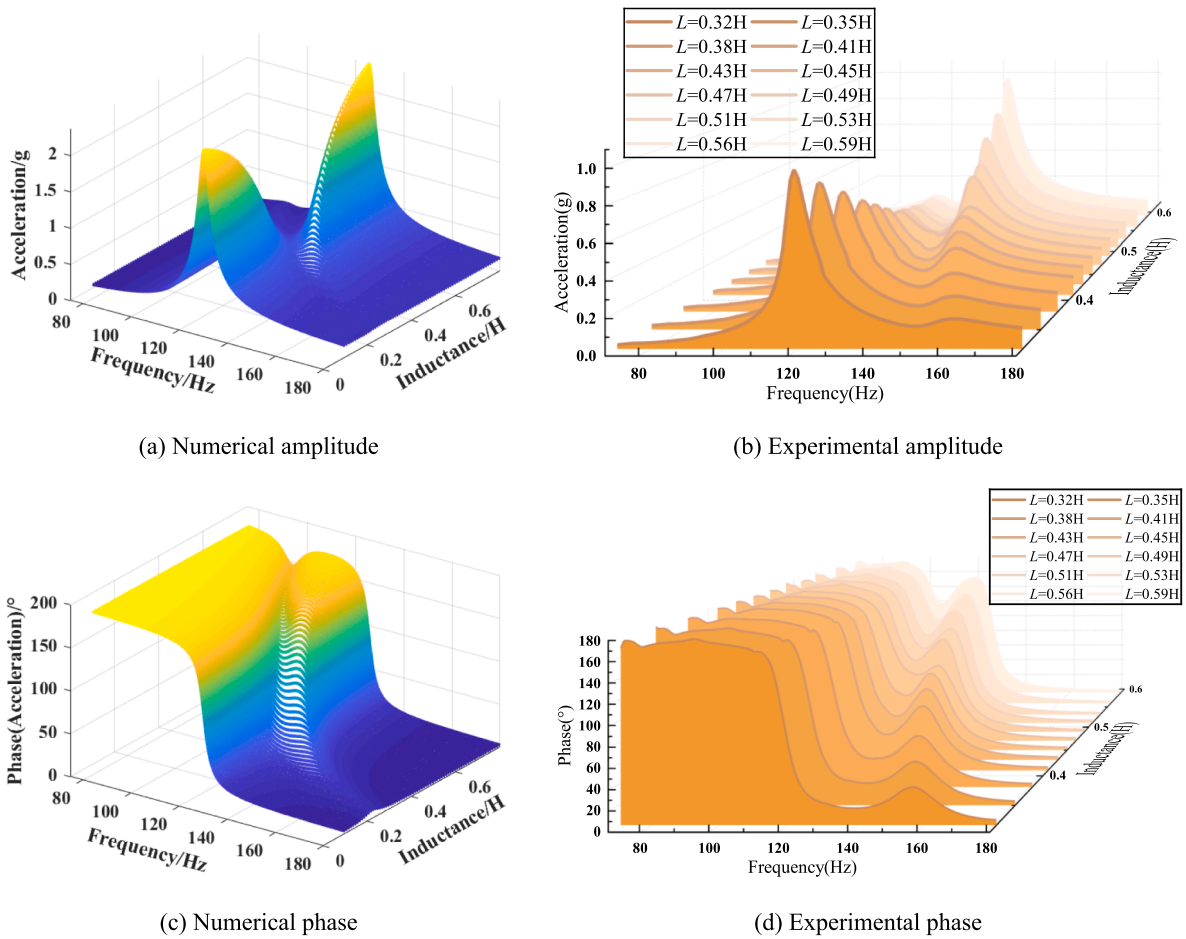


(a) Numerical amplitude (b) Experimental amplitude

(c) Numerical phase (d) Experimental phase

**Fig. 8.** Acceleration frequency response of the host system.

summarized it in Figs. 11 and 12, as shown below.

Fig. 11 visually illustrates the variation trend of the vibration reduction effect for the designed PSVA on acceleration response and force transmissibility with changing inductance. As observed in (a) and (b), the trends in the changes of acceleration and force transmissibility are consistent. As the inductance value increases from 0.3H, the reduction effect improves, reaching its optimal performance at 0.47H. Subsequently, the reduction effect begins to deteriorate. Moreover, the experimental and simulated trends align: in the vicinity of the optimal solution, the suppression effects are similar. However, when the inductance value deviates from the optimum, the experimental performance gradually surpasses the simulated results.

Additionally, another significant parameter worthy of discussion is the resonant frequency. Due to the introduction of the piezoelectric shunting circuit, the system response exhibits a two-peak nature, necessitating attention to two resonant frequencies. As depicted in Fig. 12, the variation trends of the two resonant frequencies with changes in inductance values are clearly discernible. Both resonant frequencies decrease with increasing inductance values. However, the key distinction lies in their rates of change. By observing the slopes of the curves, it becomes apparent that, for the larger resonant frequency, it initially decreases rapidly with increasing inductance until reaching the optimal inductance, after which the rate of decrease slows. Conversely, the smaller resonant frequency exhibits an initial slow decrease, followed by an accelerated descent rate after reaching the optimal inductance.

The previous research on vibration absorbers often separated the goals of vibration attenuation and isolation, with one type of absorber achieving only one of these objectives. However, the discussion above, supported by both simulation and experimental perspectives, comprehensively validates that the designed PSVA excels in both attenuation and isolation, achieving optimal performance of 80 % or more. Furthermore, the compact size and easy installation of the PSVA, as demonstrated in this study, broaden its applicability, making it adaptable to various installation environments and vibration reduction requirements in practical engineering environments. Subsequent parameter analysis focused on both amplitude and phase frequency response, revealing the trends influenced by inductance values. This insight can serve as valuable guidance for practical applications, enhancing our understanding of the impact of inductance values on amplitude and phase frequency response in practical conditions.

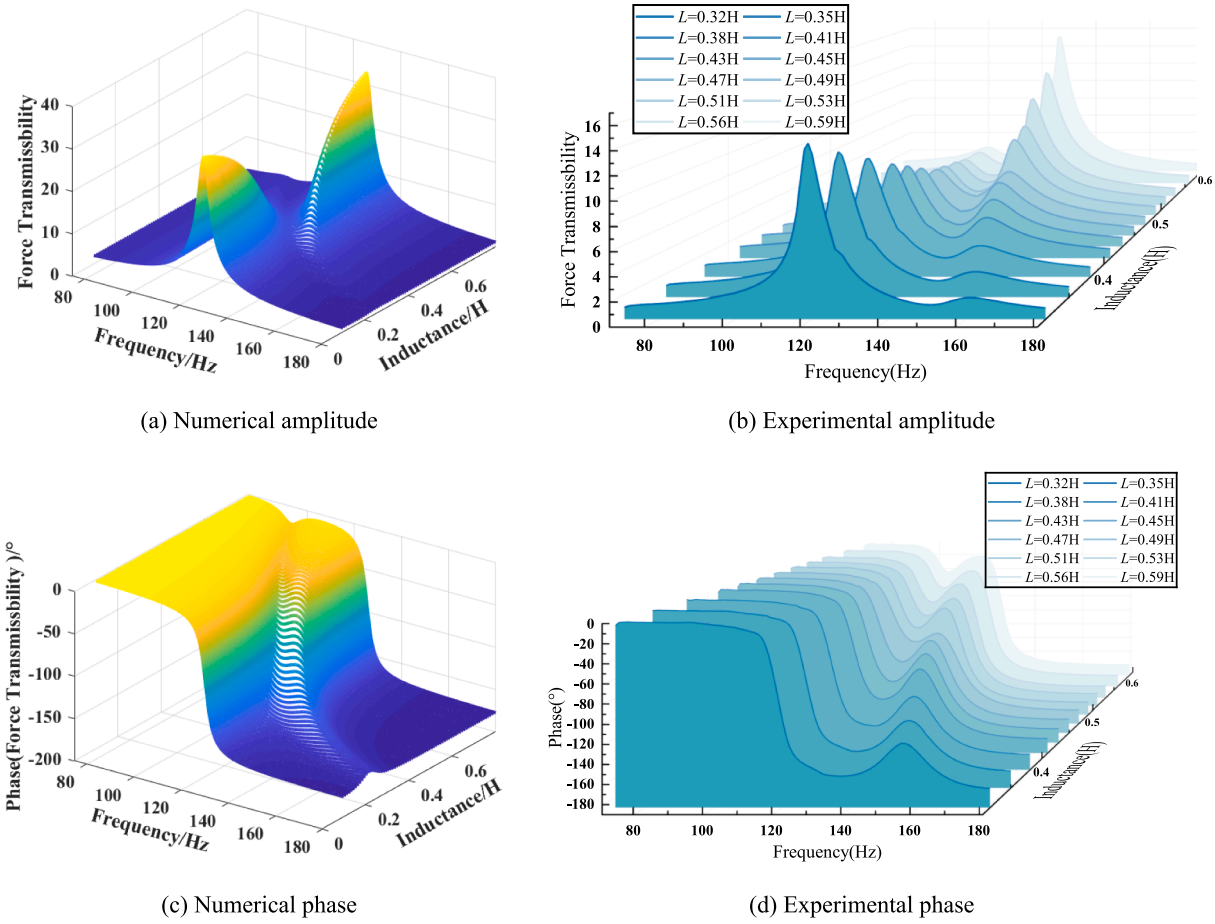


(a) Numerical amplitude (b) Experimental amplitude

(c) Numerical phase (d) Experimental phase

**Fig. 9.** Force transmissibility frequency response of the host system.

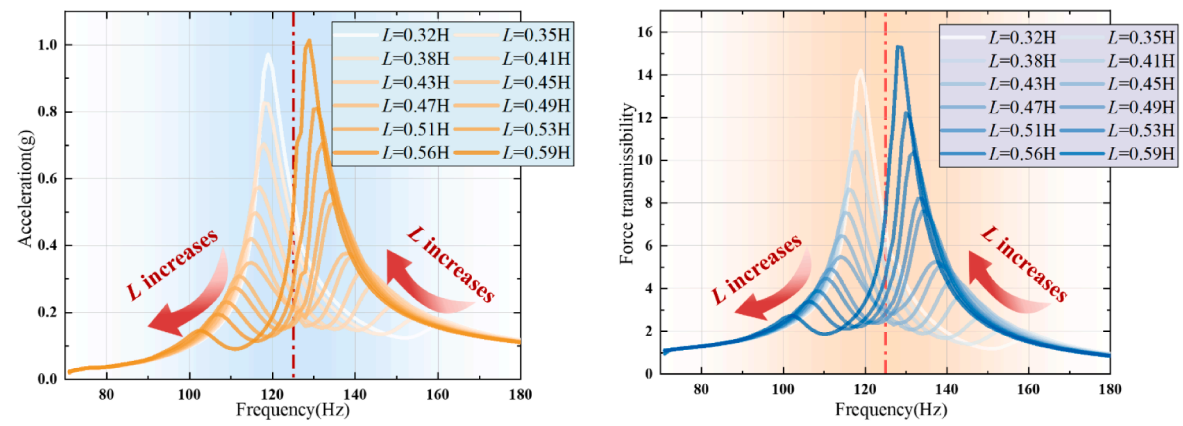


(a) Acceleration (b)Force transmissibility

**Fig. 10.** 2D plot of the response under different inductances conditions.

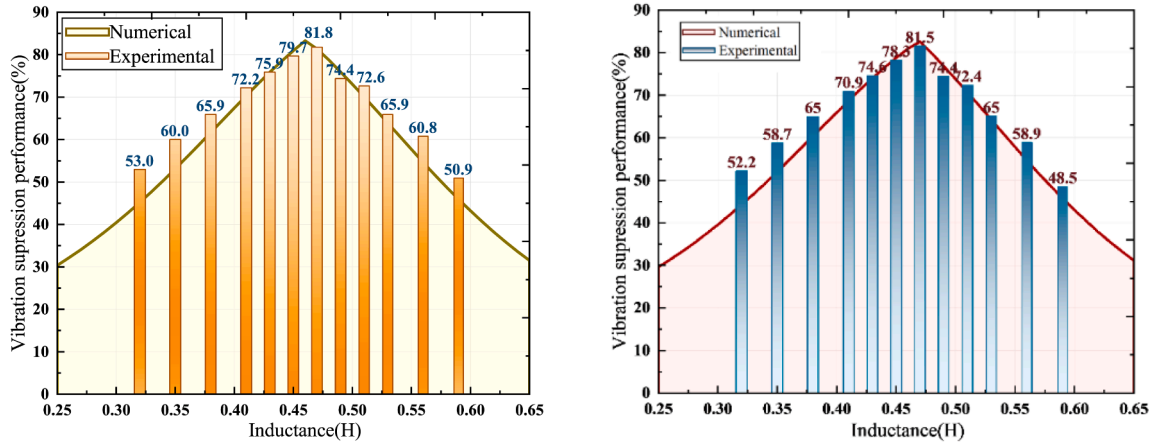


(a) Acceleration (b) Force transmissibility

**Fig. 11.** The vibration reduction effect of the designed PSVA as the function of inductance.

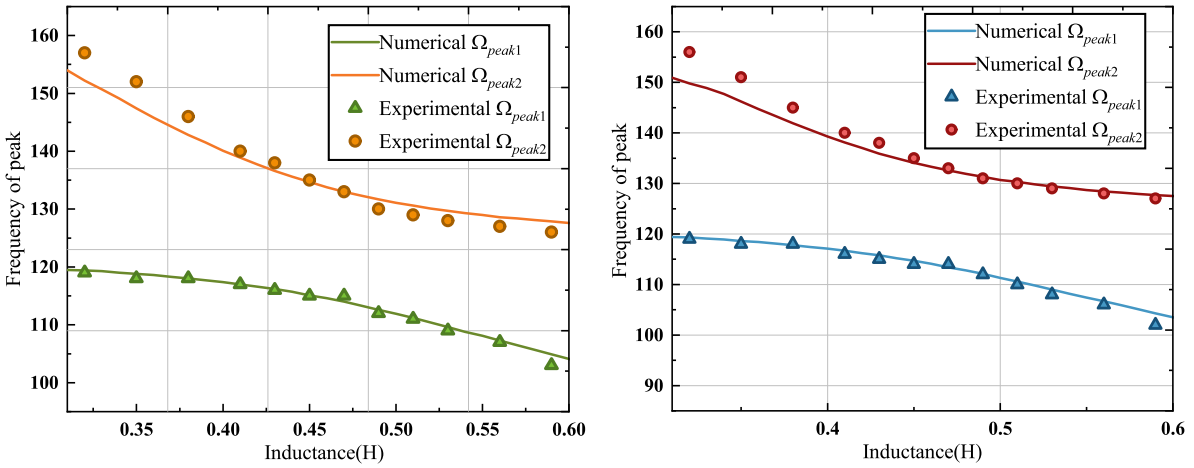


(a) Acceleration(line: numerical, dot: experimental) (b) Force transmissibility(line: numerical, dot: experimental)

**Fig. 12.** The two resonance frequencies (green & blue: smaller one, orange & red: bigger one) as a function of inductance. (For interpretation of the references to color in this figure legend, the reader is referred to the web version of this article.)

## 5. Time domain performance of designed PSVA

In this section, the time history responses of the system under random excitation, impact excitation, and sinusoidal excitation are tested to further evaluate PSVA's vibration control performance.

### *5.1. Sinusoidal excitation*

This Section focuses on the vibration control performance of the PSVA under single-frequency sinusoidal excitation in the experiment. The excitation amplitude is set at 5 N, with excitation frequencies corresponding to the resonance frequency of 124 Hz, as well as frequencies of 122 Hz, 128 Hz, and 114 Hz (gradually deviating from the resonance frequency). During the excitation process, the circuit changes from the open-circuit state to the optimal-circuit state, thereby testing the performance of PSVA under different excitation frequencies. Time domain response of acceleration and force transmissibility under these different excitation conditions are illustrated as Figs. 13-14 show. The vibration control efficiency, which is abbreviated as VCE, is defined by the following expression:

$$\mathrm{VCE} = \frac{X_{\text{open circuit}} - X_t}{X_{\text{open circuit}}} \times 100\% \tag{35}$$

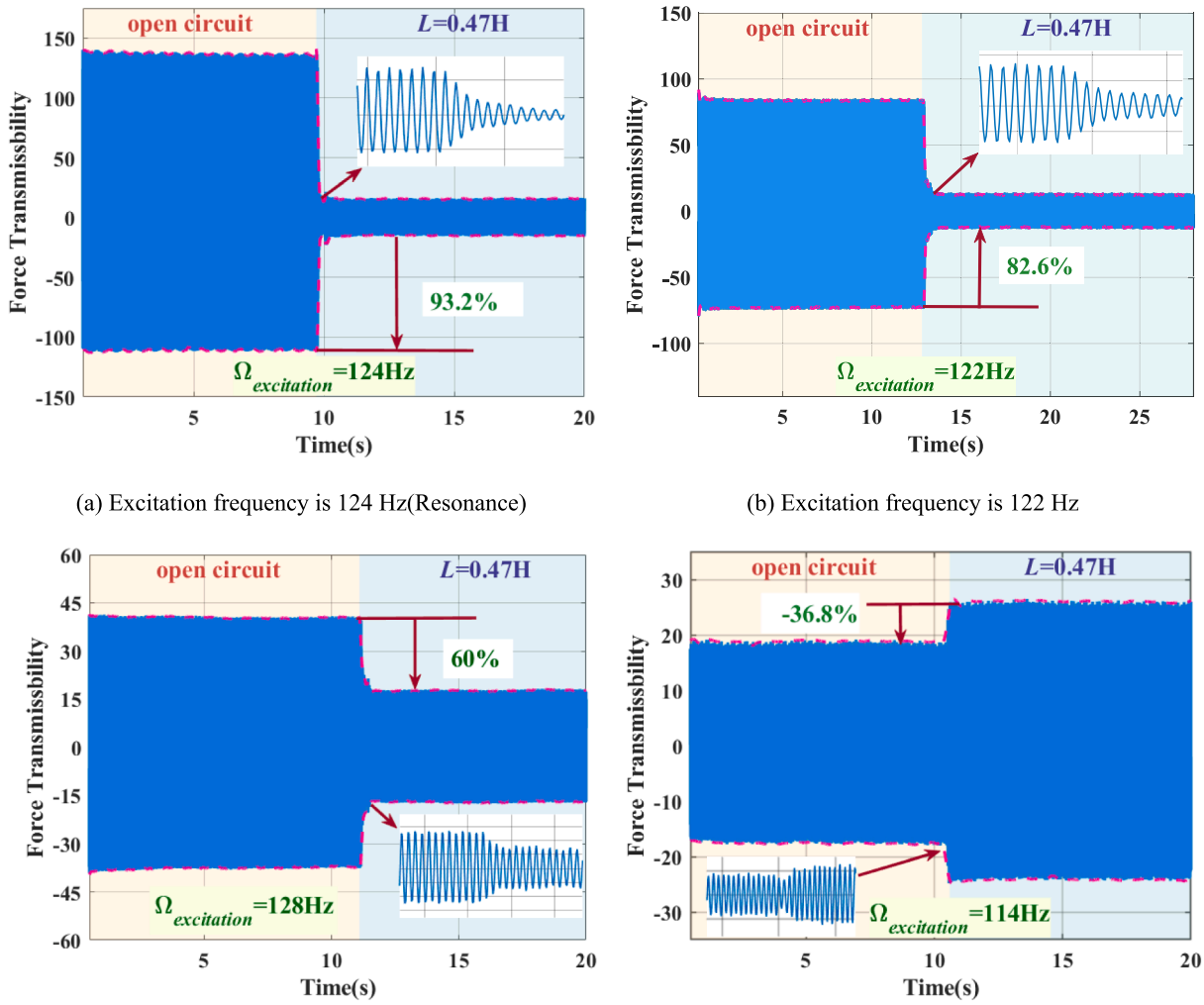


(a) Excitation frequency is 124 Hz(Resonance)

(b) Excitation frequency is 122 Hz

(c) Excitation frequency is 128 Hz

(d) Excitation frequency is 114 Hz

**Fig. 13.** Time domain response of force transmissibility, the shunting circuit condition is yellow region: open circuit, blue region: optimal circuit ($L$=0.47H). (For interpretation of the references to color in this figure legend, the reader is referred to the web version of this article.)

where $X_{\text{open circuit}}$ is the amplitude of the response under the open-circuit condition. $X_t$ is the amplitude of the response under the optimal-circuit condition. The calculated vibration control effectiveness are concluded in Table 2 and Table 3.

As shown in Fig. 13(a)-(c) and 14(a)-(c), the vibration amplitudes of the system have decreased after connecting the optimal circuit, indicating that the designed PSVA is effective under single-frequency excitation conditions. It is noteworthy that as the excitation frequency moves away from the resonance frequency, the degree of decrease in response amplitude gradually diminishes. When the excitation frequency shifts from 124 Hz (resonant frequency) to 128 Hz, the force transmissibility control effectiveness decreases from 93.2 % to 60 %, and the acceleration control effectiveness drops from 94.6 % to 64.2 %. Even at a significantly distant excitation frequency of 114 Hz, the system's response increases with the circuit connection, as depicted in Fig. 13(d) and 14(d). The acceleration control efficiency is negative. The force transmissibility increased by 36.8 % while the acceleration response increased by 83.3 %. This implies that as the excitation frequency deviates from the resonance frequency under single-frequency excitation, the vibration control efficiency of PSVA gradually deteriorates, and there may even be a counteractive effect leading to an increase in system response. This phenomenon is also clearly evident in the frequency domain response in Fig. 4 of Section 4.1. For convenience, we present it again here as Fig. 15 shows. Only during the range of [117, 136] Hz, the designed PSVA works. In frequency bands outside this range, PSVA will increase the system response and have a counterproductive effect.

This is a situation that should be avoided in practical applications. However, past research has predominantly focused on suppressing vibrations within the resonance region, with little attention given to the non-resonance region due to its relatively weak vibration amplitudes. To enhance the effectiveness of the presented PSVA over a broader frequency range, further optimization or

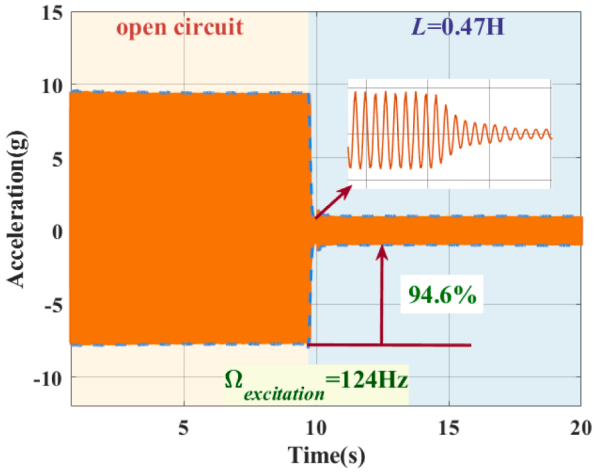


(a) Excitation frequency is 124 Hz(Resonance)

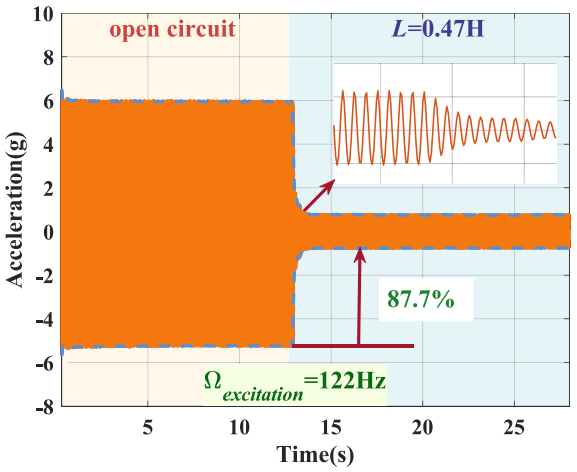


(b) Excitation frequency is 122 Hz

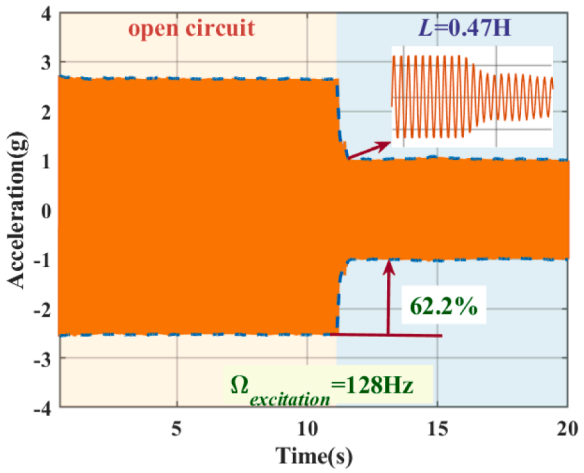


(c) Excitation frequency is 128 Hz

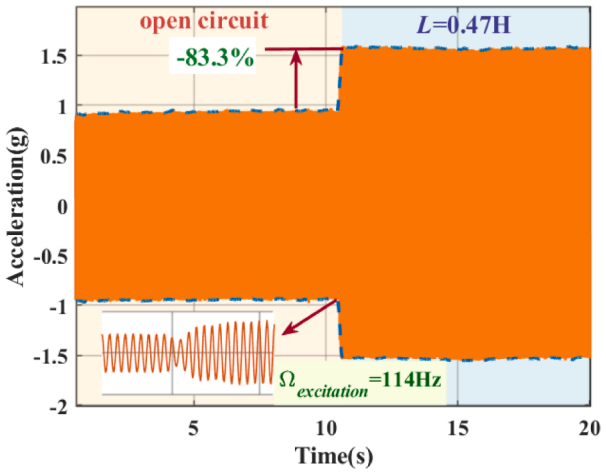


(d) Excitation frequency is 114 Hz

**Fig. 14.** Time domain response of acceleration, the shunting circuit condition is yellow region: open circuit, blue region: optimal circuit($L$=0.47H). (For interpretation of the references to color in this figure legend, the reader is referred to the web version of this article.)

**Table 2**
VCE of force transmissibility under different excitation frequencies when circuit is optimal.

| Excitation frequency | VCE |
|---|---|
| 124 Hz | 93.2 % |
| 122 Hz | 82.6 % |
| 12 8 Hz | 60 % |
| 114 Hz | −36.8 % |

adjustment of PSVA parameters may be necessary to ensure its efficiency in controlling system vibrations at different excitation frequencies.

### 5.2. Random excitation

The above discussion primarily revolves around the performance of the designed PSVA under frequency sweep excitation. However, in practical applications, various types of excitations may be encountered. To comprehensively validate the vibration control

**Table 3**
VCE of acceleration under different excitation frequencies when the circuit is optimal.

| Excitation frequency | VCE |
|---|---|
| 124 Hz | 94.6 % |
| 122 Hz | 87.7 % |
| 128 Hz | 62.2 % |
| 114 Hz | −83.3 % |

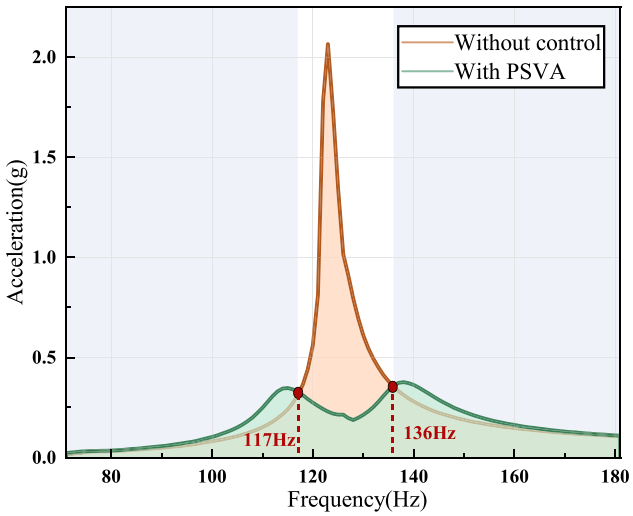


**Fig. 15.** Acceleration amplitude response, purple region: the PSVA produces a reverse effect; blue region: the PSVA works. (For interpretation of the references to color in this figure legend, the reader is referred to the web version of this article.)

performance of the designed PSVA from different perspectives, the following will discuss its effects under single-frequency sinusoidal excitation, impulse excitation, and random excitation.

Initially, the performance of the designed PSVA under random excitation is discussed. Figs. 16 and 18 respectively illustrate the time-domain responses of acceleration and force transmissibility in four different states. These states correspond to open-circuit condition, $L$=0.35H state, $L$=0.47H state, and $L$=0.59H state. The bottom-left corner features a local zoom-in around 31 s, aimed at providing a clearer view of the differences in response among the four curves. The darkest curve represents the open-circuit state, and as the color lightens, the inductance values approach the optimal solution, with the lightest color indicating the optimal solution. From the comparison of the four curves, it can be observed that as the curve color lightens, the time-domain response weakens, indicating an improving performance of the designed PSVA. The bottom-right insets of Figs. 16 and 18 clearly show that when the circuit is in the optimal state, the effect is pronounced, with the controlled response almost consistently lower than the open-circuit response within the test time range. Subsequently, to comprehensively analyze the performance of the PSVA, the commonly used evaluation functions, Power Spectral Density (PSD) and Root Mean Square (RMS) values of random responses, are obtained to assess the frequency and amplitude characteristics of the response. The PSD curves of the force transmissibility and the acceleration are presented in Fig. 17(a) and 19(a) respectively, and the RMS curves of the force transmissibility and the acceleration are shown in Fig. 17(b) and 19(b) separately.

The PSD curves in Fig. 17(a) and 19(a) effectively illustrate the frequency characteristics of the response. The resonance peak in the open-circuit state is located at 124 Hz, consistent with the earlier analysis. Under the optimal-circuit condition, the values of the two peaks are nearly the same. The frequency variations corresponding to the double peaks induced by adding the circuit are also similar to the previous analysis: as the inductance increases, both peak frequencies decrease. Simultaneously, in practical applications, the RMS value is a commonly used measure for assessing the effective strength of a signal. The RMS curves in Fig. 17(b) and 19(b) aptly showcase the amplitude characteristics of the response. As the curve colors lighten, indicating the circuit approaching the optimal state, the effective strength of the response decreases. This implies that the vibration control effect of PSVA improves, whether in terms of vibration attenuation or isolation. In order to more clearly illustrate the intensity of the random vibration, the standard deviation of the response is calculated, as shown in Tables 2 and 3. The formula for calculating the standard deviation is given as

$$s = \sqrt{\frac{1}{n-1}\sum_{i=1}^{n}\left(x_i - \frac{1}{n}\sum_{i=1}^{n}x_i\right)^2} \tag{36}$$

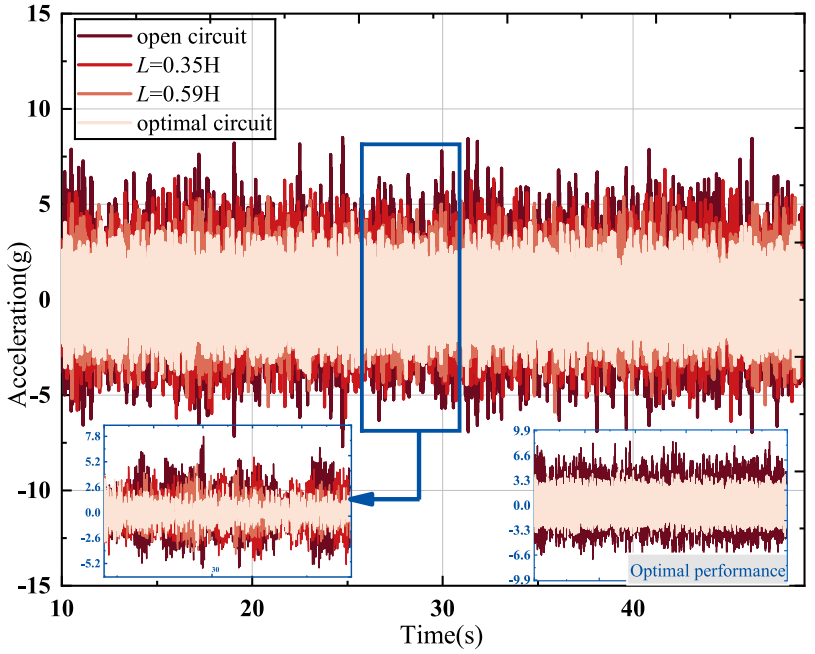


**Fig. 16.** Time domain response of acceleration under different conditions, the bottom-left corner displays a local zoom-in around 30 s, the bottom-right corner is a comparison between the open circuit state and the optimal circuit state.

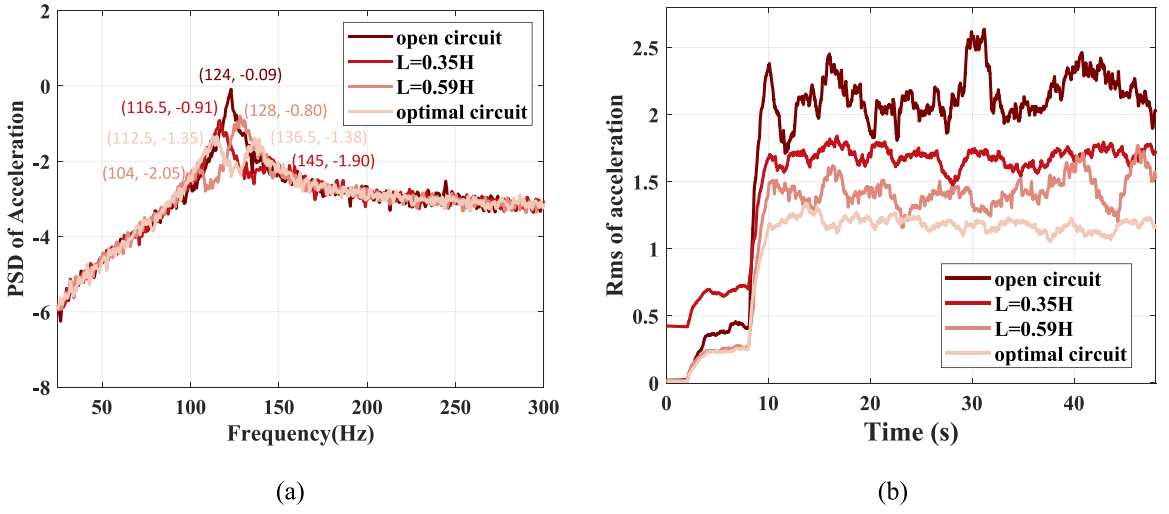


**Fig. 17.** (a) PSD curve, (b) RMS curve of force transmissibility under different conditions.

where $n$ is the number of data points, $x_i$ is $i$th data point.

Meanwhile, the VCE is defined by the following expression:

$$\mathrm{VCE} = \frac{s_{\text{open circuit}} - s_a}{s_{\text{open circuit}}} \times 100\% \tag{37}$$

where $s_a$ is the standard deviation corresponding to the circuit state to be calculated. The vibration control effectiveness are also calculated and demonstrated in Table 4 and Table 5. From Table 4, it is clear that when the inductance $L$ is optimal, the standard deviation of the acceleration response is 17.196, which is significantly lower than the standard deviation of 32.687 under open-circuit conditions, indicating excellent vibration reduction with an effectiveness of 47.4 %. As the inductance value deviates from the optimal state, the standard deviation of the response increases, approaching that of the open-circuit condition, and the computed vibration

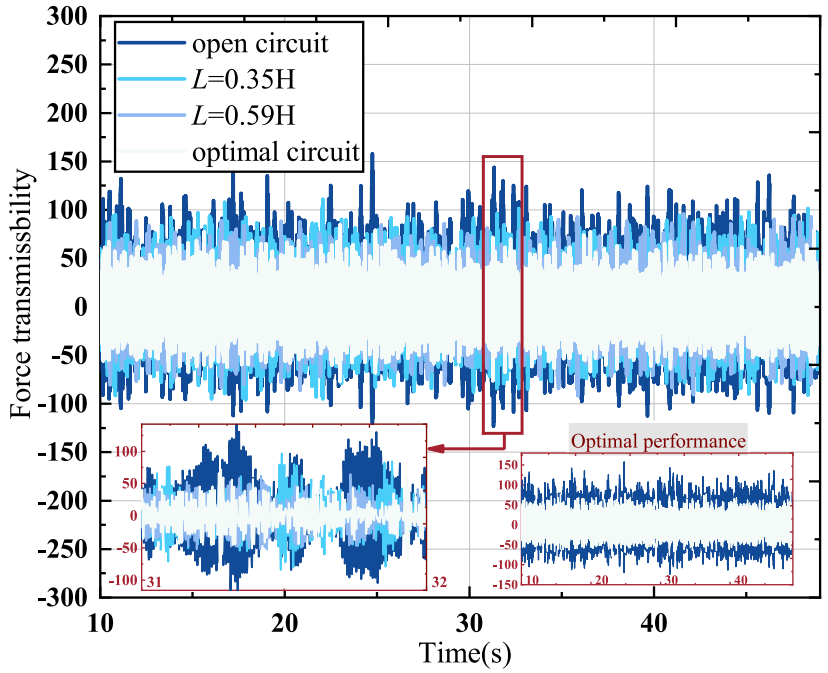


**Fig. 18.** Time domain response of force transmissibility under different conditions, the bottom-left corner displays a local zoom-in around 31 s, the bottom-right corner is a comparison between the open circuit and the optimal circuit state.

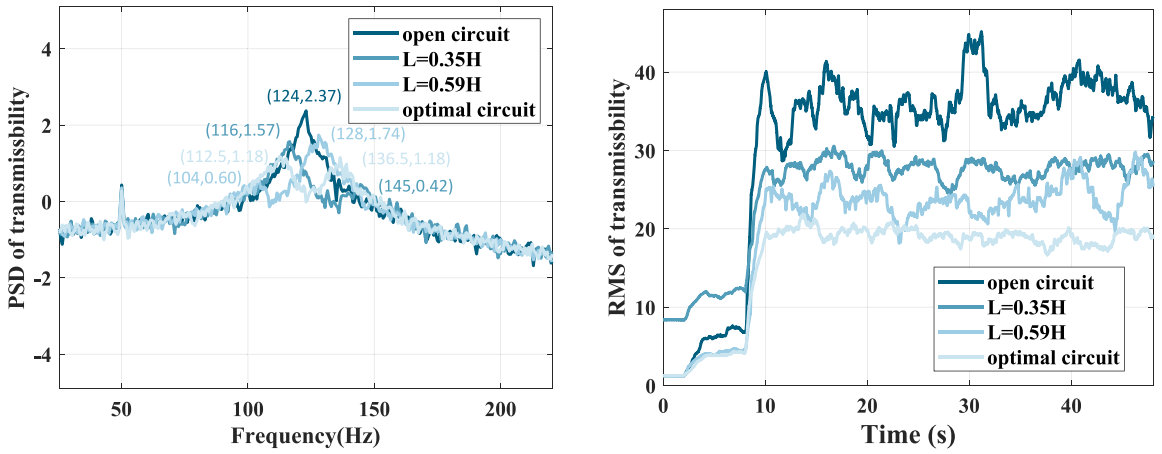


**Fig. 19.** (a) PSD curve, (b) RMS curve of force transmissibility under different conditions.

**Table 4**
Standard deviation and VCE of acceleration under random excitation in different conditions.

| Circuit State | Standard Deviation *s* | VCE |
|---|---|---|
| Open circuit | 2.311 | / |
| *L*=0.35H | 1.678 | 27.4 % |
| *L*=0.59H | 1.469 | 36.4 % |
| Optimal circuit(*L*=0.47H) | 1.184 | 48.8 % |

**Table 5**
Standard deviation and VCE of transmissibility under random excitation in different conditions.

| Circuit state | Standard deviations *s* | VCE |
|---|---|---|
| Open circuit | 32.687 | / |
| *L*=0.35H | 24.664 | 24.5 % |
| *L*=0.59H | 21.534 | 34.1 % |
| Optimal circuit(*L*=0.47H) | 17.196 | 47.4 % |

control effectiveness deteriorates. Similarly, the conclusions regarding the force transmissibility can also be obtained from the analysis presented in Table 5.

In summary, based on the analysis above, it can be concluded that under the influence of PSVA, the effective magnitudes of both the acceleration and force transmissibility are reduced substantially. Therefore, it is evident that the designed PSVA exhibits a commendable vibration suppression effect against vibrations induced by random excitations.

### 5.3. Impact excitation

Impact excitations are widely encountered in practical engineering, such as the bumps from vehicles on roads or collisions of ships on bridges, bumps during takeoff, landing, or turbulence during the processes of flight, etc. Addressing the vibration issues caused by these impacts is crucial for ensuring traffic safety and enhancing aerospace technology. In experiments, force hammers are often employed to simulate impact excitations. The time-domain responses of acceleration and force transmissibility obtained from the tests are shown in Figs. 20 and 21, with different colored curves representing various circuit conditions. The thumbnails in the bottom right corner of Fig. 20(a) and 21(a) compare the time-domain responses between the optimal circuit and the open-circuit state.

Typically, the two key indicators for evaluating the response to impact excitations are the peak magnitude and the attenuation rate. As evident in the optimal performance charts, connecting the optimal circuit results in a significant reduction not only in the peak responses of acceleration and force transmissibility compared to the open-circuit state but also in a faster attenuation. The entire vibration amplitude is effectively suppressed. Additionally, considering both Fig. 20(a) and (b), Fig. 21(a) and (b), the performance of the PSVA follows the same pattern as the variation of *L*, consistent with the earlier analysis. As the inductance approaches the optimal value, the performance gradually improves, while moving away from the optimal state leads to a decline in effectiveness. To present the effect more clearly, the decay rate metric has been chosen for analysis. The response under the impact excitation can be fitted by using the following equation

$$x(t) = Ae^{-\zeta\omega_0 t}\cos(\omega_0 t + \varphi) \tag{38}$$

where $A$ is amplitude, $\zeta$ is damping ratio, $\omega_0$ is natural frequency and $\varphi$ represents phase. By fitting the experimental response data with this equation, the abovementioned parameters can be calculated. Then, according to Ref. [38], the decay rates $\delta$ can be defined by the following expression:

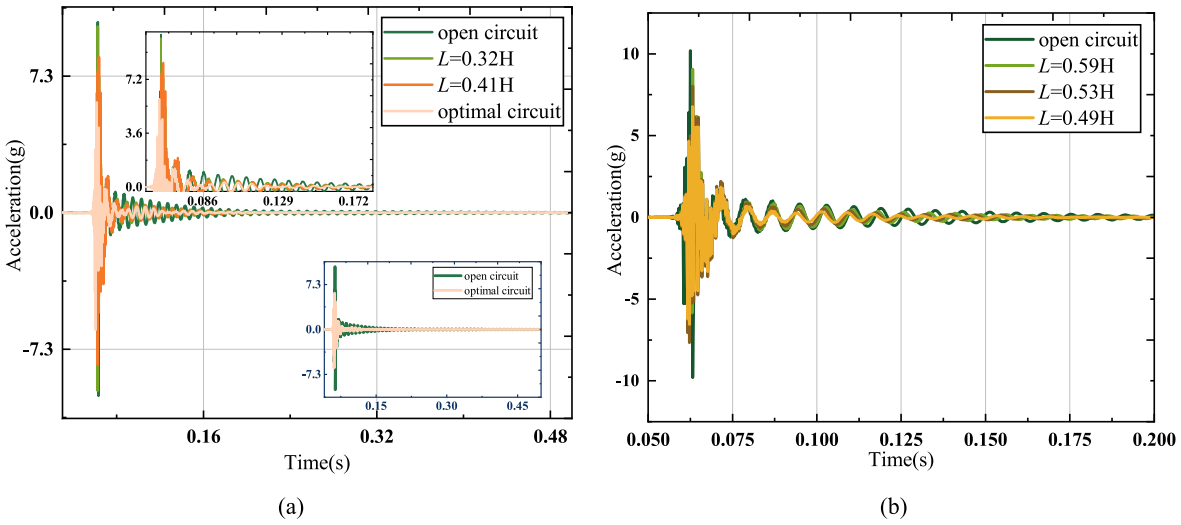


**Fig. 20.** Time domain response of acceleration under the impact acceleration when the shunting circuit is in a different state: (a)open circuit, *L*=0.32H, *L*=0.41H,optimal circuit;(b) open circuit, *L*=0.59H, *L*=0.53H, *L*=0.49H.

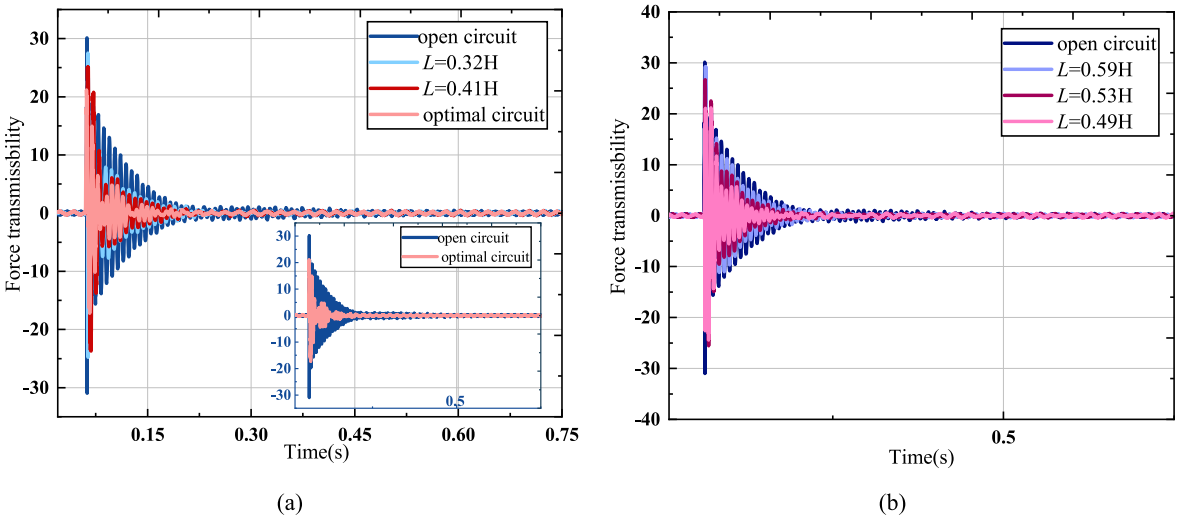


**Fig. 21.** Time domain response of force transmissibility under the impact acceleration when the shunting circuit is in a different state: (a)open circuit, $L$=0.32H, $L$=0.41H, optimal circuit;(b) open circuit, $L$=0.59H, $L$=0.53H, $L$=0.49H.

$$\delta = \frac{2\pi\zeta}{\sqrt{1-\zeta^2}} \tag{39}$$

Hence, by substituting the value of $\zeta$ into Eq. (39), the decay rates $\delta$ under different circuit conditions can be determined as Table 6 and Table 7 shows. The VCE of the PSVA under impact conditions can be represented by the increase in the system's response decay rate $\delta$ compared to the open-circuit state, as shown below

$$\mathrm{VCE} = \frac{\delta_t - \delta_{\text{open circuit}}}{\delta_{\text{open circuit}}} \times 100\% \tag{40}$$

where $\delta_t$ is the decay rate corresponding to the circuit state to be calculated.

Table 6 clearly shows that at the optimal state, the acceleration response decay rate is 0.3497, which is significantly higher than the 0.1283 decay rate observed under open-circuit conditions. This represents a notable improvement in the decay rate and a 172.56 % enhancement in vibration control efficiency. As the inductance value deviates from the optimal level, the decay rate decreases, approaching that of the open-circuit condition, and the efficiency of vibration control deteriorates. Similar conclusions regarding the force transmissibility can be drawn from the analysis in Table 7.

## 6. Design of a novel circuit

As mentioned in Section 5.1, the vibration control efficiency of PSVA gradually deteriorates, and there may even be a counteractive effect leading to an increase in system response as the excitation frequency deviates from the resonance frequency under single-frequency excitation. Meanwhile, as Fig. 15 shows, only within the resonant region, the designed PSVA works. In frequency bands outside this range, PSVA will increase the system response and have a counterproductive effect. The limitation of the PSVA urgently needs to be addressed. The existing effective solution involves an adaptive circuit to address this issue. The strategy of this adaptive circuit involves real-time adjustment of the center frequency with the excitation frequency. While this adaptive circuit theoretically and initially achieves vibration reduction effect across the entire frequency range as Ref. [34] shows, practical applications encounter various challenges. For instance, the adjustment in the adaptive control process takes a certain amount of time, introducing a time delay. The adaptive shunt circuit needs adjustment at every frequency point, and the accumulated time delay throughout the excitation

**Table 6**
Decay rate and VCE of acceleration under impact excitation in different circuit conditions.

| Circuit State | Decay Rate $\delta$ | VCE |
|---|---|---|
| $L$=0H(Open circuit) | 0.1283 | / |
| $L$=0.32H | 0.2064 | 60.87 % |
| $L$=0.41H | 0.3113 | 142.63 % |
| $L$=0.47H(Optimal circuit) | 0.3497 | 172.56 % |
| $L$=0.49H | 0.2632 | 105.14 % |
| $L$=0.53H | 0.2379 | 85.42 % |
| $L$=0.59H | 0.1842 | 43.57 % |

**Table 7**
Decay rate and VCE of transmissibility under impact excitation in different circuit conditions.

| Circuit State | Decay Rate $\delta$ | VCE |
|---|---|---|
| $L$ = 0H (Open circuit) | 0.1308 | / |
| $L$ = 0.32H | 0.2430 | 85.77 % |
| $L$ = 0.41H | 0.3843 | 193.81 % |
| $L$ = 0.47H (Optimal circuit) | 0.4647 | 255.28 % |
| $L$ = 0.49H | 0.3173 | 142.58 % |
| $L$ = 0.53H | 0.2574 | 96.79 % |
| $L$ = 0.59H | 0.1989 | 34.24 % |

process results in the final stages deviating from the expected standards, thereby failing to achieve the anticipated damping effect. Moreover, complex circuit control systems also bring additional weight and installation space requirements, which is undesirable. Therefore, a better and easier method is needed to broaden the vibration control bandwidth.

According to the discussion in Section 4.2, we know that the smaller the inductor, the better it performs in the higher frequency band, and conversely, the larger the inductor performs better in the lower frequency band. According to this result, the optimal vibration control effects are achieved at excitation frequencies of 128 Hz and 114 Hz by adjusting the shunt circuit in the experimental process. From Figs. 22 and 23, it can be observed that with an inductance of 0.41H at an excitation frequency of 128 Hz, the damping effect of PSVA on acceleration response increased from the original 62.2 % to 70.2 %, and the damping effect on force transmissibility increased from the original 60 % to 75 %. With an inductance of 0.59H at an excitation frequency of 114 Hz, the damping effect of PSVA on acceleration response increased from the original −83.3 % to 55.2 %, and the vibration control effect on force transmissibility increased from the original −36.8 % to 47.3 %. PSVA demonstrates excellent vibration suppression effects in the new circuit states.

Therefore, inspired by the above analysis, a novel circuit called segmented inductance circuit is proposed as Fig. 24 shows in the following section to broaden the vibration suppression bandwidth, enhancing the versatility of PSVA. By varying the inductance only at the $\Omega_A$ (122 Hz) and $\Omega_B$ (132 Hz) as shown in Fig. 25, ideally, not only can excellent vibration reduction like the purple region shows be achieved across the entire frequency range, but it also mitigates the effects of time delay.

Then the test was conducted to verify these thoughts. Initially, the inductance L is 0.62H, adjusted to 0.47H at 122 Hz and 0.25H at 132 Hz. The acceleration frequency response under this condition is exhibited in Fig. 26. Obviously, the frequency response is suppressed between the frequency domain [75, 180] Hz. Compared to the fact that the effective operating frequency range of a typical *RL* circuit is [117, 136] Hz, the introduction of segmented inductance significantly expands the effective bandwidth of the designed PSVA, thereby improving the performance of the designed PSVA. It should be noted that this study primarily introduces the concept of segmented inductance. Hence, the inductance is manually adjusted in the test at two key frequency points to achieve the segmented inductor effect. In future research or practical applications, it is feasible to consider using band-pass filters (BPF) to control and adjust the inductance. The BPF is an electronic filter that allows signals within a specific frequency range to pass through while blocking signals that are higher or lower than that range. By utilizing its frequency selectivity, the proposed segmented inductance can be effectively realized. In practical applications, each of the three circuit branches depicted in Fig. 24 is equipped with a BPF. The pass-

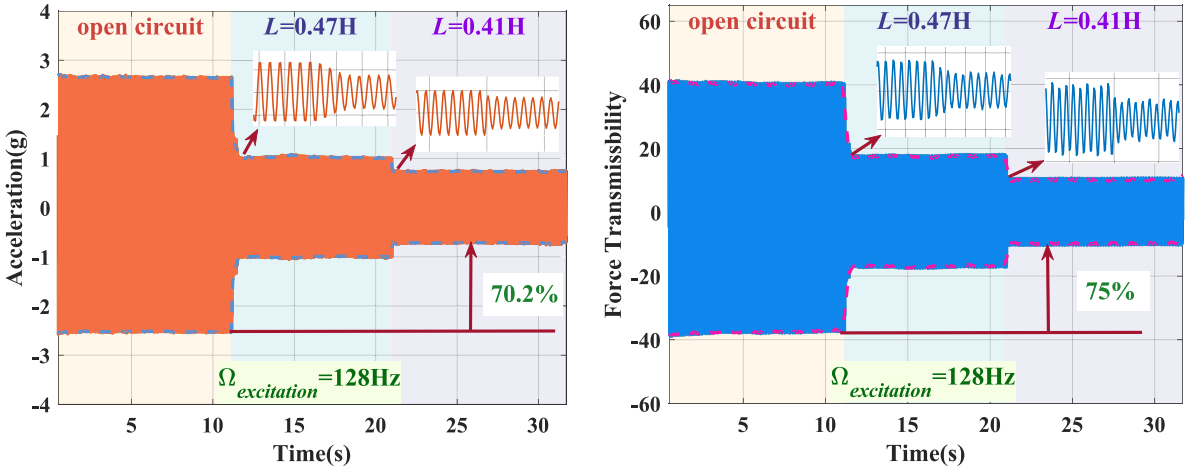


(a) Acceleration (b) Force transmissibility

**Fig. 22.** Time domain response when the excitation frequency is 128 Hz, the shunting circuit condition is yellow region: open circuit, blue region: $L$=0.47H, purple region: $L$=0.41H. (For interpretation of the references to color in this figure legend, the reader is referred to the web version of this article.)

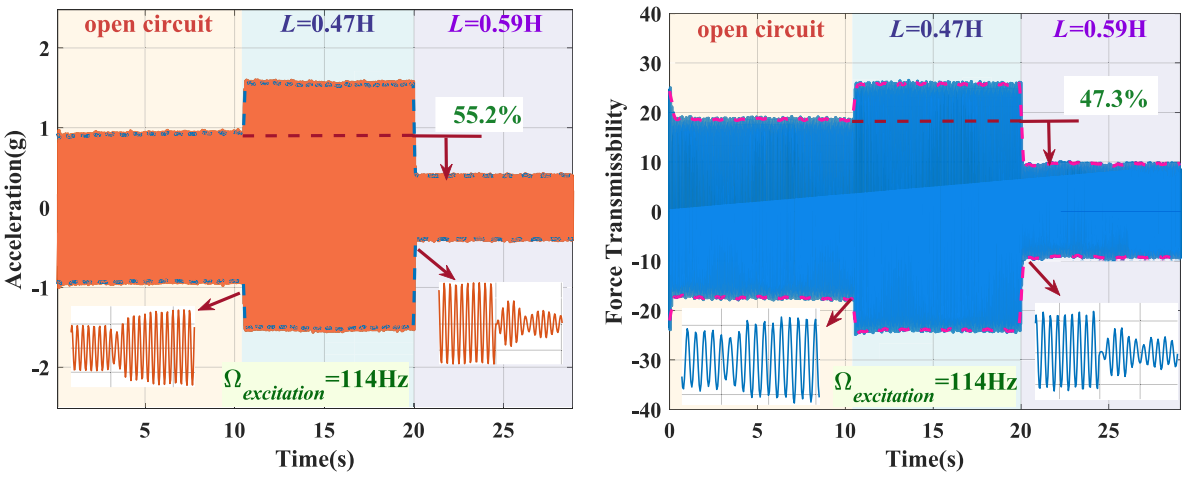


(a) Acceleration (b) Force transmissibility

**Fig. 23.** Time domain response when the excitation frequency is 114 Hz, the shunting circuit condition is yellow region: open circuit, blue region: $L$=0.47H, purple region: $L$=0.41H.

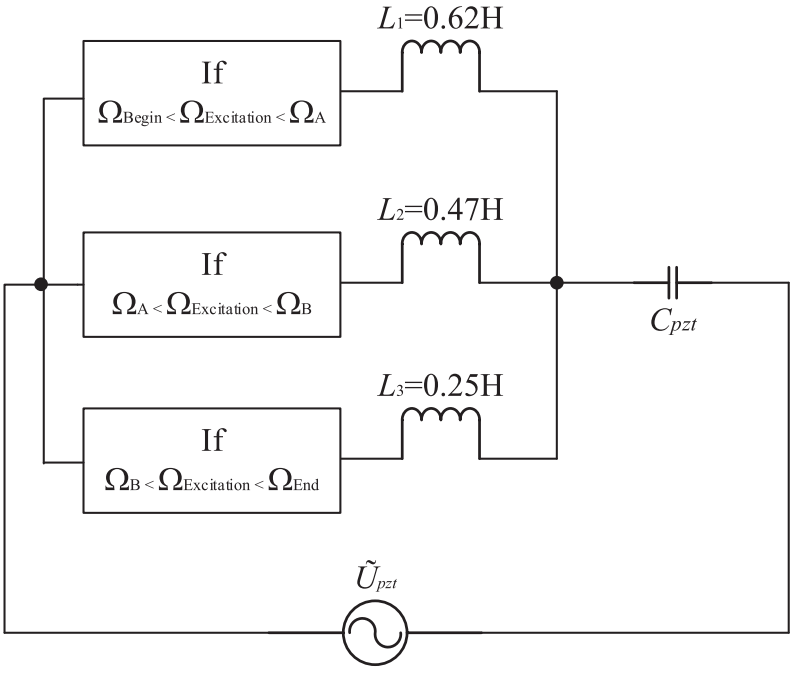


**Fig. 24.** Schematic diagram of segmented inductance.

band settings for these BPFs are configured corresponding to the frequency ranges indicated in the boxes for each branch. When the sweep excitation is applied, only the branch where the excitation frequency falls within the pass-band of its corresponding BPF will allow current to pass through; otherwise, that branch will be open-circuited. Therefore, within the specific excitation frequency range, only the branch with the relevant inductance will be active, while the other branches will be open-circuited., thereby successfully achieving segmented inductance.

## 7. Conclusion

A novel PSVA is proposed here and successfully applied to a single DOF system. This proposed PSVA is composed of a butterfly-

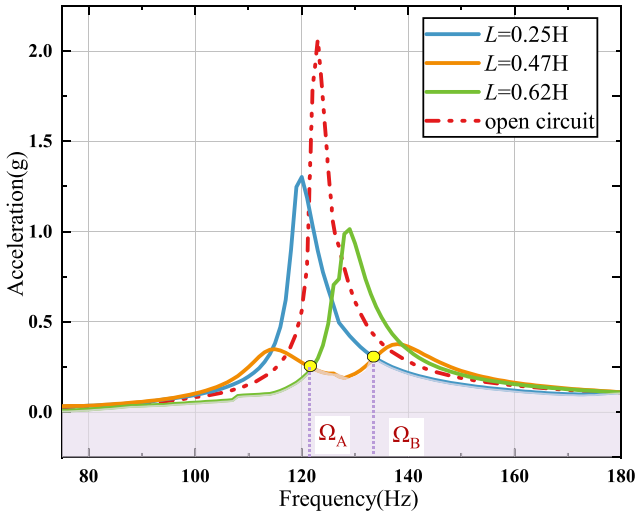


**Fig. 25.** Experimental acceleration response of the host system under conditions of different *L*.

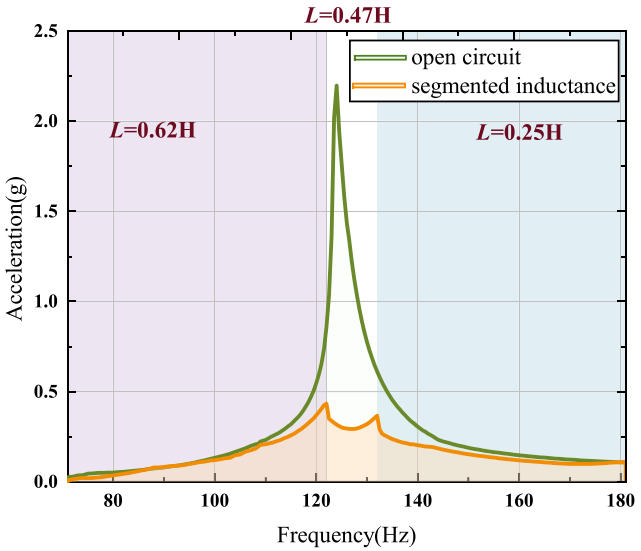


**Fig. 26.** The experimental performance of the designed PSVA connected to the segmented inductance circuit.

shaped steel frame and a piezoelectric stack. A simplified dynamic model of this electromechanical coupling system was established, and its numerical acceleration response and force transmissibility frequency response were obtained. A test system containing masses and designed PSVA was designed and manufactured. A sweep sine test was conducted. By contrasting open-circuit and connected-circuit states, the designed PSVA exhibits outstanding performance numerically and experimentally both in amplitude reduction and vibration isolation. Following that, more excitation conditions containing random excitation, impact excitation, and single-frequency excitation were imposed in tests to comprehensively demonstrate the versatility of the designed PSVA. The parameter analysis process also summarizes the impact of inductance values on the effectiveness of vibration control, providing valuable guidance for the practical application of PSVA. Subsequently, inspired by single-frequency tests, a segmented inductance circuit is proposed to broaden the effective vibration control bandwidth of PSVA, and its efficacy is well-validated through experiment.

## CRediT authorship contribution statement

**Weiting Chen:** Writing – original draft, Visualization, Software, Formal analysis, Data curation. **Jiayu Lu:** Software, Resources, Formal analysis, Data curation. **Xing Tan:** Writing – review & editing, Validation, Methodology. **Paolo Albertelli:** Writing – review & editing, Validation. **Huan He:** Supervision, Project administration, Funding acquisition, Conceptualization.

## Declaration of competing interest

The authors declare that they have no known competing financial interests or personal relationships that could have appeared to influence the work reported in this paper.

## Data availability

Data will be made available on request.

## Acknowledgments

This work is supported by National Natural Science Foundation of China (Grant No.12072153), Funding for Outstanding Doctoral Dissertation in NUAA (Grant No. BCXJ22–01) and China Scholarship Council, which are greatly appreciated.

## References

[1] X. Shi, T. Chen, J. Zhang, B. Su, Q. Cong, W. Tian, A review of bioinspired vibration control technology, Appl. Sci. 11 (2021), https://doi.org/10.3390/app112210584.
[2] R. Kandasamy, F. Cui, N. Townsend, C.C. Foo, J. Guo, A. Shenoi, Y. Xiong, A review of vibration control methods for marine offshore structures, Ocean Eng. 127 (2016) 279–297, https://doi.org/10.1016/j.oceaneng.2016.10.001.
[3] P. Gao, T. Yu, Y. Zhang, J. Wang, J. Zhai, Vibration analysis and control technologies of hydraulic pipeline system in aircraft: A review, Chin. J. Aeronaut. 34 (2021) 83–114, https://doi.org/10.1016/j.cja.2020.07.007.
[4] J. Sheikhi, M. Fathi, Natural Rubber Bearing Incorporated with Steel Ring Damper (NRB-SRD), Int. J. Steel Struct. 20 (2020) 23–34, https://doi.org/10.1007/s13296-019-00267-7.
[5] H. Kim, S. Yoshitomi, M. Tsuji, I. Takewaki, Post-tensioning high-hardness rubber damper system for vibration control of residential houses and building structures, Adv. Struct. Eng. 15 (2012) 2157–2172, https://doi.org/10.1260/1369-4332.15.12.2157.
[6] A.M. Mandani, F. Hejazi, A. Nikkhoo, Development of hybrid rubber damper-restrainer (HRDR) system for structures under sever dynamic excitation, Structures 55 (2023) 1354–1387, https://doi.org/10.1016/j.istruc.2023.06.106.
[7] X. Kang, Q. Huang, Z. Wu, J. Tang, X. Jiang, S. Lei, A Review of the Tuned Mass Damper Inerter (TMDI) in Energy Harvesting and Vibration Control: Designs, Analysis and Applications, Comput. Model. Eng. Sci. 139 (2024) 2361–2398, https://doi.org/10.32604/cmes.2023.043936.
[8] J.W. Baker, Measuring bias in structural response caused by ground motion scaling, Pacific Conf. Earthq. Eng. (2007) 1–6, https://doi.org/10.1002/eqe.
[9] H. Garrido, O. Curadelli, D. Ambrosini, Improvement of tuned mass damper by using rotational inertia through tuned viscous mass damper, Eng. Struct. 56 (2013) 2149–2153, https://doi.org/10.1016/j.engstruct.2013.08.044.
[10] Y. Hu, M.Z.Q. Chen, Z. Shu, L. Huang, Analysis and optimisation for inerter-based isolators via fixed-point theory and algebraic solution, J. Sound Vib. 346 (2015) 17–36, https://doi.org/10.1016/j.jsv.2015.02.041.
[11] Y. Hu, M.Z.Q. Chen, Performance evaluation for inerter-based dynamic vibration absorbers, Int. J. Mech. Sci. 99 (2015) 297–307, https://doi.org/10.1016/j.ijmecsci.2015.06.003.
[12] S. Manzoni, A. Argentino, F. Lucà, M. Berardengo, M. Vanali, SMA-based adaptive tuned mass dampers: Analysis and comparison, Mech. Syst. Signal Process. 186 (2023) 109883, https://doi.org/10.1016/j.ymssp.2022.109883.
[13] X. Gao, J. Yang, J. Wu, X. Xin, Z. Li, X. Yuan, X. Shen, S. Dong, Piezoelectric Actuators and Motors: Materials, Designs, and Applications, Adv. Mater. Technol. 5 (2020) 1–26, https://doi.org/10.1002/admt.201900716.
[14] H. Jin, X. Gao, K. Ren, J. Liu, L. Qiao, M. Liu, W. Chen, Y. He, S. Dong, Z. Xu, F. Li, Review on Piezoelectric Actuators Based on High-Performance Piezoelectric Materials, IEEE Trans. Ultrason. Ferroelectr. Freq. Control 69 (2022) 3057–3069, https://doi.org/10.1109/TUFFC.2022.3175853.
[15] J. Wang, C. Zhang, S. Gu, K. Yang, H. Li, Y. Lai, D. Yurchenko, Enhancement of low-speed piezoelectric wind energy harvesting by bluff body shapes: Spindle-like and butterfly-like cross-sections, Aerosp. Sci. Technol. 103 (2020) 105898, https://doi.org/10.1016/j.ast.2020.105898.
[16] Y. Wang, D.J. Inman, A survey of control strategies for simultaneous vibration suppression and energy harvesting via piezoceramics, J. Intell. Mater. Syst. Struct. 23 (2012) 2021–2037, https://doi.org/10.1177/1045389X12444485.
[17] J.A.B. Gripp, D.A. Rade, Vibration and noise control using shunted piezoelectric transducers: A review, Mech. Syst. Signal Process. 112 (2018) 359–383, https://doi.org/10.1016/j.ymssp.2018.04.041.
[18] E.M. Qureshi, X. Shen, J.J. Chen, Vibration control laws via shunted piezoelectric transducers: A review, Int. J. Aeronaut. Sp. Sci. 15 (2014) 1–19, https://doi.org/10.5139/IJASS.2014.15.1.1.
[19] S. Sassi, J. Renno, H. Zhou, A. Baz, Experimental Investigation of the Vibration Control of Nonrotating Periodic Drill Strings, J. Vib. Acoust. 143 (2021) 1–13, https://doi.org/10.1115/1.4049942.
[20] K. Billon, N. Montcoudiol, A. Aubry, R. Pascual, F. Mosca, F. Jean, C. Pezerat, C. Bricault, S. Chesné, Vibration isolation and damping using a piezoelectric flextensional suspension with a negative capacitance shunt, Mech. Syst. Signal Process. 140 (2020), https://doi.org/10.1016/j.ymssp.2020.106696.
[21] W. Sheng, H. Xiang, A piezoelectric tuned mass damper for simultaneous vibration control and energy harvesting, Smart Mater. Struct. 33 (2024), https://doi.org/10.1088/1361-665X/ad1317.
[22] W. Sheng, H. Xiang, Z. Zhang, X. Yuan, High-efficiency piezoelectric energy harvester for vehicle-induced bridge vibrations: Theory and experiment, Compos. Struct. 299 (2022) 116040, https://doi.org/10.1016/j.compstruct.2022.116040.
[23] X. Wang, Z. Shi, Double piezoelectric energy harvesting cell: Modeling and experimental verification, Smart Mater. Struct. 26 (2017), https://doi.org/10.1088/1361-665X/aa6cf9.
[24] Y. Jian, G. Hu, L. Tang, Y. Shen, Y. Zhan, K. Aw, Adaptive piezoelectric metamaterial beam: autonomous attenuation zone adjustment in complex vibration environments, Smart Mater. Struct. 32 (2023), https://doi.org/10.1088/1361-665X/acf62f.
[25] O. Alfahmi, C. Sugino, A. Erturk, Duffing-type digitally programmable nonlinear synthetic inductance for piezoelectric structures, Smart Mater. Struct. 31 (2022), https://doi.org/10.1088/1361-665X/ac858b.
[26] S. Manzoni, M. Berardengo, F. Boccuto, M. Vanali, Piezoelectric-shunt-based approach for multi-mode adaptive tuned mass dampers, Mech. Syst. Signal Process. 200 (2023) 110537, https://doi.org/10.1016/j.ymssp.2023.110537.
[27] O. Alfahmi, A. Erturk, Programmable hardening and softening cubic inductive shunts for piezoelectric structures: Harmonic balance analysis and experiments, J. Sound Vib. 571 (2024) 118029, https://doi.org/10.1016/j.jsv.2023.118029.
[28] C. Liu, R. Zhao, K. Yu, H.P. Lee, B. Liao, A quasi-zero-stiffness device capable of vibration isolation and energy harvesting using piezoelectric buckled beams, Energy 233 (2021) 121146, https://doi.org/10.1016/j.energy.2021.121146.
[29] C. Liu, R. Zhao, K. Yu, H.P. Lee, B. Liao, Simultaneous energy harvesting and vibration isolation via quasi-zero-stiffness support and radially distributed piezoelectric cantilever beams, Appl. Math. Model. 100 (2021) 152–169, https://doi.org/10.1016/j.apm.2021.08.002.
[30] X. Sun, F. Wang, J. Xu, Nonlinear Piezoelectric Structure for Ultralow-frequency Band Vibration Energy Harvesting with Magnetic Interaction, Int. J. Precis. Eng. Manuf. - Green Technol. 6 (2019) 671–679, https://doi.org/10.1007/s40684-019-00117-1.

[31] K. Guo, Y. Xu, Random vibration suppression of a truss core sandwich panel using independent modal resonant shunt and modal criterion, Appl. Sci. 7 (2017), https://doi.org/10.3390/app7050496.
[32] H. Ji, Y. Guo, J. Qiu, Y. Wu, C. Zhang, C. Tao, A new design of unsymmetrical shunt circuit with negative capacitance for enhanced vibration control, Mech. Syst. Signal Process. 155 (2021), https://doi.org/10.1016/j.ymssp.2020.107576.
[33] L.F. Lin, Z.Q. Lu, L. Zhao, Y.S. Zheng, H. Ding, L.Q. Chen, Vibration isolation of mechatronic metamaterial beam with resonant piezoelectric shunting, Int. J. Mech. Sci. 254 (2023), https://doi.org/10.1016/j.ijmecsci.2023.108448.
[34] J. Paixão, E. Foltête, E. Sadoulet-Reboul, G. Chevallier, S. Cogan, Self-adaptive piezoelectric vibration absorber with semi-passive tunable resonant shunts, J. Sound Vib. 583 (2024) 118424, https://doi.org/10.1016/j.jsv.2024.118424.
[35] G.M. Chatziathanasiou, N.A. Chrysochoidis, C.S. Rekatsinas, D.A. Saravanos, A semi-active shunted piezoelectric tuned-mass-damper for multi-modal vibration control of large flexible structures, J. Sound Vib. 537 (2022) 117222, https://doi.org/10.1016/j.jsv.2022.117222.
[36] P. Soltani, G. Kerschen, G. Tondreau, A. Deraemaeker, Piezoelectric vibration damping using resonant shunt circuits: An exact solution, Smart Mater. Struct. 23 (2014), https://doi.org/10.1088/0964-1726/23/12/125014.
[37] K. Yamada, H. Matsuhisa, H. Utsuno, K. Sawada, Optimum tuning of series and parallel LR circuits for passive vibration suppression using piezoelectric elements, J. Sound Vib. 329 (2010) 5036–5057, https://doi.org/10.1016/j.jsv.2010.06.021.
[38] W.T. Thomson, Theory of vibration with applications, fourth edition, Theory Vib. with Appl. Fourth Ed. (2018) 1–546. https://doi.org/10.1201/9780203718841.